

2

# AD-A278 544 PAGE

Form Approved  
OMB No. 0704-0188

Public reporting burden for this collection of information is estimated to average 1 hour per response, including the time for reviewing instructions, searching existing data sources, gathering and reviewing the data, collecting the data, reviewing and collecting the data, and reviewing and collecting the data.



Do not release, including the time for reviewing instructions, searching existing data sources, gathering and reviewing the data, collecting the data, reviewing and collecting the data, and reviewing and collecting the data. Send comments regarding this burden estimate or any other aspect of this collection of information, including suggestions for reducing the burden, to Washington Headquarters Services, Directorate for Information Operations and Reports, 1215 Jefferson Ave., Washington, DC 20540.

1. AGENCY USE ONLY (Leave blank)	2. REPORT DATE 3/31/94	3. REPORT TYPE AND DATES COVERED FINAL; 1/15/91 to 1/14/94
----------------------------------	---------------------------	---

4. TITLE AND SUBTITLE Final report for "Multiparameter Radar and Aircraft Based Studies of Microphysical, Kinematic and Electrical Structure of Convective Clouds During CaPE".	5. FUNDING NUMBERS 61102F 2310 <i>AC</i>
--	---

6. AUTHOR(S) V. N. Bringi
------------------------------

7. PERFORMING ORGANIZATION NAME(S) AND ADDRESS(ES) Colorado State University Dept. of Electrical Engineering Fort Collins, CO 80523	8. PERFORMING ORGANIZATION REPORT NUMBER AFOSR-91-0141 AFOSR-TR- 94 0246
--	--

9. SPONSORING/MONITORING AGENCY NAME(S) AND ADDRESS(ES) AFOSR/NL 110 Duncan Ave, Suite B115 Bolling AFB, DC 20332-0001 MA: James T. Kroll	10. SPONSORING/MONITORING AGENCY REPORT NUMBER
---	--

11. SUPPLEMENTARY NOTES
-------------------------

**DTIC ELECTE**  
**S G D**  
APR 25 1994

12a. DISTRIBUTION/AVAILABILITY STATEMENT APPROVED FOR PUBLIC RELEASE; DISTRIBUTION UNLIMITED	12b. DISTRIBUTION CODE
---	------------------------

13. ABSTRACT (Maximum 200 words) <p>Two storms from the 9 August, 1991 CaPE case were analyzed in-depth focusing on multiparameter radar signature evolution over 60 min. in coordination with 24 aircraft penetrations which provided particle image and electric field data together with vertical air motion, cloud water and other state parameters. A total of five discrete "cells" were identified in the two storms and their life cycle fully documented. Collaboration with South Dakota School of Mines and University of Alabama at Huntsville has resulted in a full integration of aircraft image and field mill data (from SDSM&amp;T T-28 aircraft) with vertical air motion from dual-Doppler wind synthesis (UAH). The cellular evolution starts with a warm rain phase where updrafts and a very low concentration of large drops dominate the cloud. As the supercooled drops rise in the updraft they freeze and acquire a water-coat possibly by collisions with other liquid drops. The multi-parameter radar signatures clearly identify this mixed-phase zone. The cloud thereafter gets electrified which may intensify to produce lightning depending on cloud vertical growth, and generation of updraft/downdrafts.</p>
---

14. SUBJECT TERMS radar, electric field, microphysics	15. NUMBER OF PAGES
DTIC QUALITY INSPECTED	16. PRICE CODE

17. SECURITY CLASSIFICATION OF REPORT <i>u</i>	18. SECURITY CLASSIFICATION OF THIS PAGE <i>u</i>	19. SECURITY CLASSIFICATION OF ABSTRACT <i>u</i>	20. LIMITATION OF ABSTRACT <i>u</i>
---	--	---	--

APR 1994

Final Report**A. Manuscripts in Preparation**

1. Bringi, V. N., A. Detwiler, K. Knupp, et al., "The microphysical kinematic and electrical evolution of warm-based Florida convective cells: The 9 August case from CaPE," in preparation for J. Appl. Meteor.
2. Bringi, V. N., L. Liu, I. J. Caylor and V. Chandrasekar, "Examples of multiparameter radar signatures from Florida storms," in preparation for J. Appl. Meteor.

**B. Reviewed Journals**

1. Liu, L., V. N. Bringi, V. Chandrasekar, E. A. Mueller and A. Mudukotore, 1994: Analysis of the copolar correlation coefficient between horizontal and vertical polarizations, J. Atmos. Ocean. Tech., in press.

**C. Conference Proceedings**

The following appeared in Preprints, 26th Int. Conf. Radar Meteor.

1. Caylor, I. J., V. Chandrasekar, V. N. Bringi and S. S. Minger, "Multiparameter radar observations of lighting."
2. Bringi, V. N., I. J. Caylor, J. Turk and L. Liu, "Microphysical and electrical evolution of a convective storm using multiparameter radar and aircraft data during CaPE."
3. Bringi, V. N., A. Detwiler, V. Chandrasekar, P. L. Smith, L. Liu, I. J. Caylor and D. Musil, "Multiparameter radar and aircraft study of the transition from early to mature storm during CaPE: The case of 9 August 1991."
4. Liu, L., V. N. Bringi, I. J. Caylor and V. Chandrasekar, "Intercomparison of multiparameter radar signatures from Florida storms."
5. Detwiler, A., J. H. Helsdon, D. J. Musil, R. Ramachandran, P. L. Smith, V. N. Bringi and I. J. Caylor, "Observations of electrification in CaPE thunderstorms," Preprints 17th Conf. Severe Local Storms/Atmos. Elec., AMS, 1993.

**D. Graduate Students**

1. Liu, L. 1993: "Remote sensing of precipitation using multiparameter radar: statistics, processing algorithms and analysis techniques," Ph.D. Dissertation, Colorado State University, Electrical Engineering, Non-US.
2. Kochar, A., 1994: "Multiparameter radar studies of Florida storms," M.S. Thesis, Colorado State University, Electrical Engineering, non-US.

94-12441



DTIC QUALITY INSPECTED 2

94 4 22 137

E. Post Doctorates

1. I. J. Caylor, Electrical Engineering, US.

F. Senior Student Project

1. S. S. Minger, "Multiparameter radar signatures of rocket triggered lightning," Electrical Engineering, 1993, US.

G. Concise Summary

Two storms from 9 August, 1991 of CaPE were analyzed, the first one being a multi-cellular complex and the second one being more compact with early identified and persistent updraft/downdraft structures. Three discrete cells from storm 1 and two cells from storm 2 were analyzed in detail from near first echo to mature stage. The first emphasis was on identification of multiparameter radar signatures such as positive differential reflectivity ( $Z_{DR}$ ) columns extending into sub-freezing temperatures of the cloud, enhanced signatures of linear depolarization ratio (LDR) "capping" the positive  $Z_{DR}$  columns, and regions of enhanced X-band specific attenuation ( $A_3$ ). New reliable algorithms for estimating LDR and  $A_3$  were developed taking into consideration antenna errors in regions of strong reflectivity gradients, propagation effects and other measurement errors. Time-height contours through the 5 cell cores were constructed for reflectivity,  $Z_{DR}$ , LDR and  $A_3$  which clearly showed the microphysical evolution. Aircraft data were also integrated within these time-height profiles after careful navigation to identify the cells penetrated by the various aircraft (4 in number) at various times and altitudes. Vertical winds from dual-Doppler analyses by Dr. Kevin Knupp of the University of Alabama at Huntsville have been integrated into the major cell of storm 1, and is being also performed for storm 2. A comprehensive manuscript is being prepared dealing with the microphysical, kinematic and electrical evolution of the two storms of 9 August. Substantial effort was devoted to careful analysis of aircraft particle image data from which particle types and size distributions were obtained. Careful consideration of navigation errors and aircraft "skin paints" enabled the construction of vertical profiles of multiparameter radar data along the aircraft tracks. The aircraft field mill data from the NCAR King Air, T-28 and P3 were carefully analyzed for self-consistency whenever the tracks penetrated the same cells at different altitudes. A consistent picture is beginning to emerge relating first cloud electrification to appearance of mixed-phase signatures in the multiparameter radar data of LDR and  $A_3$ . However, persistent updraft/downdraft regions appear necessary to produce, in addition, electric fields strong enough to produce lightning discharges. While the transition from early, warm cloud to mature phase is rather dramatically apparent from examination of positive  $Z_{DR}$  columns followed by LDR "cap" and enhanced attenuation near  $-5^{\circ}\text{C}$  level, the strengthening of the electric field leading to first lightning is typically delayed by a further 5-10 minutes to allow for charge separation to occur which appears to be substantially accelerated by up/down vertical air motions. A careful analysis of the dual-Doppler synthesized vertical and horizontal winds is being performed to understand the microphysical-kinematic-electrical evolution and linkages therein.

Dr. I. J. Caylor has been spearheading analysis of multiparameter radar signatures in known cases of natural and triggered lightning. The orientation of ice crystals in regions of strong electrical fields has been vividly captured via the increase in S-band specific differential phase ( $K_{DP}$ ) followed by a reduction to near zero after lightning discharge (crystals dis-oriented). The cyclical nature of  $K_{DP}$  correlated with lightning discharges confirms McCormick and Hendry's experimental observations of nearly two decades earlier using circular polarization at K-band. Multiparameter radar signatures of rocket triggered lightning has been analyzed using polarimetric and dual-

frequency reflectivity measurements at S and X-bands. These results are being further analyzed and the number of cases expanded so that some generalizations can be arrived at for both natural and triggered lightning.

Accession For	
NTIS CRA&I	<input checked="" type="checkbox"/>
DTIC TAB	<input type="checkbox"/>
Unannounced	<input type="checkbox"/>
Justification .....	
By .....	
Distribution /	
Availability Codes	
Dist	Avail and/or Special
A-1	

## Analysis of the Copolar Correlation Coefficient between Horizontal and Vertical Polarizations

L. LIU, V. N. BRINGI, V. CHANDRASEKAR, E. A. MUELLER, AND A. MUDUKUTORE

Colorado State University, Fort Collins, Colorado

(Manuscript received 20 May 1993, in final form 19 November 1993)

### ABSTRACT

Recent research has suggested that the copolar correlation coefficient termed  $\rho_{hv}(0)$  can be used to identify large hail and improve polarization estimates of rainfall. The typical measured values of  $\rho_{hv}(0)$  at S band vary approximately between 0.8 and 1.0. For applications to hail identification, the required accuracy should be within  $\pm 0.01$ , while for rainfall improvement a higher accuracy is necessary, for example, within  $\pm 0.001$ . The statistics of the estimator of  $\rho_{hv}(0)$  using the Gaussian spectrum approximation from both an analytical approach and using simulations are discussed. The standard deviation and bias in  $\hat{\rho}_{hv}(0)$  are computed as a function of number of samples, Doppler spectral width, and mean value of  $\rho_{hv}(0)$ . The effect of finite signal-to-noise ratio and phase noise are also studied using simulations. Several other estimators of  $\rho_{hv}(0)$  are evaluated. Time series data collected with the Colorado State University CHILL radar are analyzed and compared with the simulations. Antenna pattern effects as they affect the accuracy of  $\hat{\rho}_{hv}(0)$  are also discussed.

### 1. Introduction

The magnitude of the zero-lag copolar correlation coefficient between horizontal- and vertical-polarized received signals, termed as  $\rho_{hv}(0)$ , has been recently investigated for application toward hail sizing, improving polarization estimates of rainfall, and detection of the melting level in both convective and stratiform precipitation (Balakrishnan and Zrnić 1990; Jameson 1989; Zrnić et al. 1993; Illingworth and Caylor 1991). A conventional differential reflectivity  $Z_{DR}$  radar, which alternately transmits horizontal- (H) and vertical- (V) polarized waves (pulse repetition time is  $T_s$ ) and receives the copolar signal (either coherently or incoherently) via a single receiver, can be used to estimate  $\rho_{hv}(0)$ . A good discussion of the various physical factors that affect this correlation are given in Balakrishnan and Zrnić (1990). Sachidananda and Zrnić (1985) were the first to consider the effect of  $\rho_{hv}(0)$  on the accuracy of the  $Z_{DR}$  measurement. By assuming a Gaussian spectrum, the estimator for  $\rho_{hv}(0)$  can be written as (Sachidananda and Zrnić 1989)

$$\hat{\rho}_{hv}(0) = \frac{\hat{\rho}_{hv}(T_s)}{[\hat{\rho}(2T_s)]^{0.25}}, \quad (1)$$

where  $\hat{\rho}(2T_s) = \hat{\rho}_{hh}(2T_s) = \hat{\rho}_{vv}(2T_s)$  (see Fig. 1). It is now well established that the standard deviations in  $Z_{DR}$  and differential propagation phase  $\Phi_{DP}$  are very

sensitive to  $\rho_{hv}(0)$ . Balakrishnan and Zrnić (1990) have given curves of the standard deviation and bias of  $\hat{\rho}_{hv}(0)$  versus the number of H-V sample pairs ( $M$ ) with Doppler spectrum width as a parameter. However, they did not provide a derivation other than stating the method used, that is, perturbation analysis following Zrnić (1977).

Illingworth and Caylor (1991) estimated  $\rho_{hv}(0)$  from time series of reflectivity data ( $Z_{hh}$  and  $Z_{vv}$ ) and showed distributions of  $\rho_{hv}(0)$  from light rainfall (drizzle) and a "bright band," the mean values being 0.997 and 0.849, respectively. They also provided a simple empirical relationship derived from data for the standard deviation of  $\rho_{hv}(0)$ . For example, for a mean  $\rho_{hv}(0)$  value of 0.99 in rainfall, the standard error is typically about 0.002. From theoretical considerations, that is, assuming a gamma drop size distribution  $N(D) = N_0 D^m \exp[-(3.67 + m)/D_0]$  and equilibrium oblate shapes, they found that a change in  $m$  from 0 to 2, at a fixed  $Z_{DR}$  value, corresponds approximately to a change in  $\rho_{hv}(0)$  by 0.002. Thus, very high accuracy in  $\hat{\rho}_{hv}(0)$  is needed if it is to be used to estimate  $m$  and thereby improve polarization estimates of rainfall (see also Jameson 1989). For hail detection and/or sizing, or for brightband detection, the simulations of Balakrishnan and Zrnić (1990) suggested that reduced accuracy ( $\sim \pm 0.01$ ) in  $\hat{\rho}_{hv}(0)$  may be sufficient.

In this paper, we derive the bias and standard deviation of  $\hat{\rho}_{hv}(0)$  given in (1) using the perturbation method (details are provided in appendix A). These results are compared with a simulation procedure first introduced by Chandrasekar et al. (1986). Several different estimators of  $\rho_{hv}(0)$  are considered and com-

Corresponding author address: Dr. V. N. Bringi, Department of Electrical Engineering, Colorado State University, Fort Collins, CO 80523.

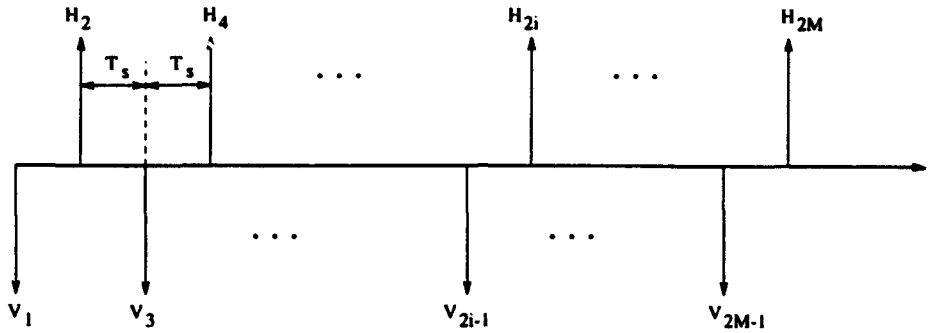


FIG. 1. Alternate copolar complex time sequence (H—horizontal; V—vertical).

pared using simulations. The effect of signal-to-noise ratio (SNR) and phase noise on the bias of  $\hat{\rho}_{hv}(0)$  are also considered. Time series data collected with the Colorado State University CHILL radar are analyzed and stratified according to the Doppler spectral shapes. The experimental standard deviations in  $Z_{DR}$ ,  $\Phi_{DP}$ , and  $\hat{\rho}_{hv}(0)$  are compared with simulations. The paper ends with some general conclusions about the achievable accuracy of  $\hat{\rho}_{hv}(0)$ .

## 2. Statistical aspects

### a. Perturbation method

The perturbation method is commonly used to derive the standard deviation of nonlinear estimators. This method has been used previously for deriving the standard deviation of Doppler velocity estimators (Zrnić 1977). We extend this method to derive the bias and standard deviation of  $\hat{\rho}_{hv}(0)$  defined in (1).

Figure 1 shows a schematic of the alternately received copolar time samples,  $H_{2i}$  and  $V_{2i+1}$ . The  $\hat{\rho}_{hv}(1)$  and  $\hat{\rho}(2)$  are defined as

$$\hat{\rho}_{hv}(1) = \frac{|\sum_{i=1}^{M-1} H_{2i} V_{2i+1}^*|}{(\sum_{i=1}^{M-1} |H_{2i}|^2 \sum_{i=1}^{M-1} |V_{2i+1}|^2)^{0.5}}, \quad (2)$$

$$\hat{\rho}(2) = \hat{\rho}_{hh}(2) = \frac{|\sum_{i=1}^{M-1} H_{2i} H_{2i+2}^*|}{\sum_{i=1}^{M-1} |H_{2i}|^2}, \quad (3)$$

which is slightly different from the estimators given by Balakrishnan and Zrnić (1990).

The bias and variance of  $\hat{\rho}_{hv}(0)$  can be expressed as (see appendix A for details)

$$\text{bias}[\hat{\rho}_{hv}(0)] = E[\hat{\rho}_{hv}(0)] - \rho_{hv}(0) = \rho_{hv}(0) \left\{ 0.15625 \frac{\text{var}[\hat{\rho}_{hh}(2)]}{\rho_{hh}^2(2)} - 0.25 \frac{\text{cov}[\hat{\rho}_{hv}(1), \hat{\rho}_{hh}(2)]}{\rho_{hv}(1)\rho_{hh}(2)} \right\}, \quad (4)$$

$$\text{var}[\hat{\rho}_{hv}(0)] = \rho_{hv}^2(0) \left\{ \frac{\text{var}[\hat{\rho}_{hv}(1)]}{\rho_{hv}^2(1)} + 0.25^2 \frac{\text{var}[\hat{\rho}_{hh}(2)]}{\rho_{hh}^2(2)} - 0.5 \frac{\text{cov}[\hat{\rho}_{hv}(1), \hat{\rho}_{hh}(2)]}{\rho_{hv}(1)\rho_{hh}(2)} \right\}, \quad (5)$$

where

$$\frac{\text{var}[\hat{\rho}_{hv}(1)]}{\rho_{hv}^2(1)} = \frac{1}{2M^2} \sum_{m=-M+1}^{M-1} (M - |m|) \left\{ \rho_{hh}^2(2m) \left[ 1 + \frac{1}{\rho_{hh}^2(1)\rho_{hv}^2(0)} \right] + \rho_{hh}^2(2m+1)\rho_{hv}^2(0) \right. \\ \left. + \text{Re} \left[ \frac{R_{hh}(2m+1)R_{hh}^*(2m-1)}{R_{hh}^2(1)} - 4 \frac{R_{hh}(2m)R_{hh}^*(2m-1)}{R_{hh}(0)R_{hh}(1)} \right] \right\}, \quad (6)$$

$$\frac{\text{var}[\hat{\rho}_{hh}(2)]}{\rho_{hh}^2(2)} = \frac{1}{M^2} \sum_{m=-M+1}^{M-1} (M - |m|) \left\{ \rho_{hh}^2(2m) \left[ 1 + \frac{1}{2\rho_{hh}^2(2)} \right] \right. \\ \left. + \text{Re} \left[ \frac{R_{hh}(2m+2)R_{hh}^*(2m-2)}{2R_{hh}^2(2)} - 2 \frac{R_{hh}(2m)R_{hh}^*(2m-2)}{R_{hh}(0)R_{hh}(2)} \right] \right\}, \quad (7)$$

$$\frac{\text{cov}[\hat{\rho}_{hv}(1), \hat{\rho}_{hh}(2)]}{\rho_{hv}(1)\rho_{hh}(2)} = \frac{1}{2M^2} \sum_{m=-M+1}^{M-1} (M - |m|) \left\{ \rho_{hh}^2(2m) + \rho_{hh}^2(2m+1)\rho_{hv}^2(0) + \text{Re} \left\{ \frac{R_{hh}(2m+2)R_{hh}^*(2m-1)}{R_{hh}(1)R_{hh}(2)} + \frac{R_{hh}(2m)R_{hh}^*(2m+1)}{R_{hh}(1)R_{hh}(2)} - \frac{R_{hh}(2m)R_{hh}^*(2m-2)}{R_{hh}(0)R_{hh}(2)} [1 + \rho_{hv}^2(0)] - 2 \frac{R_{hh}(2m)R_{hh}^*(2m-1)}{R_{hh}(0)R_{hh}(1)} \right\} \right\}, \quad (8)$$

and under the Gaussian spectral assumption  $\rho_{hh}(m)$  and  $R_{hh}(m)$  can be written as

$$\rho_{hh}(m) = \exp[-8(m\pi\sigma_v T_s/\lambda)^2],$$

$$R_{hh}(m) = R_{hh}(0)\rho_{hh}(m) \exp(-j4m\pi\bar{v}T_s/\lambda).$$

Note that  $\bar{v}$  and  $\sigma_v$  are the mean and spectral width of the Doppler spectrum,  $\lambda$  is the wavelength,  $M$  is the number of H-V pairs, and  $\rho_{hv}(0)$  is the true mean.

The bias predicted by (4) is very small for typical values of  $M$  used in current research radars (bias is less than 0.001 when  $M = 64$ ,  $\lambda/4T_s = 26.75 \text{ m s}^{-1}$ ,  $\rho_{hv}(0) = 0.95$ , and  $\sigma_v \leq 4 \text{ m s}^{-1}$ ). Figure 2 shows the predicted standard deviation of  $\hat{\rho}_{hv}(0)$  using (5) versus (a)  $M$  and (b)  $\rho_{hv}(0)$ . In (a)  $\sigma_v = 3 \text{ m s}^{-1}$  and  $\rho_{hv}(0)$  is a parameter, while in (b)  $M = 128$  with  $\sigma_v$  as a parameter. Figure 2b shows that the standard deviation decreases more or less linearly with increasing  $\rho_{hv}(0)$ , a result deduced empirically by Illingworth and Caylor (1991) from their data. Their experimentally deduced standard deviations in rainfall with  $Z_{DR}$  in the range of 0–3 dB are less than 0.004, which lies between the curves for  $\rho_{hv}(0) = 0.98$  and 0.995 in Fig. 2a. However, it should be added that their  $\hat{\rho}_{hv}(0)$  estimates were based on time series of power samples using an interpolation algorithm that they showed to be nearly identical to the power sample equivalent of (1).

*b. Simulations*

Chandrasekar et al. (1986) have developed a spectral domain procedure for simulating the bivariate time series of the horizontally and vertically polarized signals given the Doppler spectrum,  $\rho_{hv}(0)$ , and  $Z_{DR}$ . Green (1990) has further extended it to the quadivariate case, that is, fully polarimetric case. The simulation technique has been used previously to study and model fluctuations in  $Z_{DR}$  and differential propagation phase,  $\Phi_{DP}$  (Chandrasekar and Bringi 1988; Chandrasekar et al. 1990; Bringi et al. 1990). We use it here to study the fluctuations in  $\hat{\rho}_{hv}(0)$  and to compare it with the perturbation method. It can also be used to study other estimators of  $\rho_{hv}(0)$  and to study the effects of SNR, phase noise, and non-Gaussian spectral shapes on the bias and variance of  $\hat{\rho}_{hv}(0)$ .

Figure 3 shows the simulation results with the same parameters as in Fig. 2 (see Chandrasekar et al. 1986;

Green 1990). Note that  $Z_{DR} = 0 \text{ dB}$  in the time series simulations since the bias and standard deviation of  $\hat{\rho}_{hv}(0)$  are independent of  $Z_{DR}$ . The bias is again very small ( $<0.001$ ) but negative (i.e., estimated values are less than the true mean). Illingworth and Caylor (1991) noticed that a slight negative bias of about 0.002 would bring good agreement between their  $\hat{\rho}_{hv}(0)$  versus  $Z_{DR}$  data and theory for rainfall. We find good agreement between the perturbation method and the simulations (cf. Figs. 2 and 3), which gives confidence in applying the simulation method to study other estimators of  $\rho_{hv}(0)$ . Simulations also show that the estimator for  $\rho_{hv}(0)$  used by Balakrishnan and Zrnić (1990) gives bias and standard deviation that are extremely close to those obtained using (2) and (3). Since (2) and (3) are computationally less intensive we prefer it to that used by Balakrishnan and Zrnić (1990).

1) OTHER ESTIMATORS OF  $\rho_{hv}(0)$

The estimator defined in (1) will be termed the *alternate* sample estimator or  $\hat{\rho}_{hv}^a(0)$ . For incoherent radars, power samples can be used to estimate  $\rho_{hv}(0)$ . Let  $p_h(2i) = |H_{2i}|^2$  and  $p_v(2i+1) = |V_{2i+1}|^2$  be the alternately received power samples as shown in the schematic of Fig. 1. The estimate of the copolar power correlation coefficient  $\hat{\rho}_{p_h, p_v}(0)$  can be written as

$$\hat{\rho}_{p_h, p_v}(0) = \frac{\hat{\rho}_{p_h, p_v}(1)}{[\hat{\rho}_{p_h, p_h}(2)]^{0.25}}. \quad (9)$$

Then,

$$\hat{\rho}_{hv}^p(0) = [\hat{\rho}_{p_h, p_v}(0)]^{0.5}. \quad (10)$$

This follows from the fact that  $\rho_p = \rho^2$ , where  $\rho_p$  stands for  $\rho_{p_h}$  or  $\rho_{p_v}$  (Doviak and Zrnić 1984). The estimator given by (10) will be termed the *power* sample estimator. This was one of the estimators used by Illingworth and Caylor (1991).

Several methods can be used to estimate the missing received signal in Fig. 1 (Chandrasekar et al. 1993) (see also Fig. 4) and in effect construct “simultaneous” samples. Illingworth and Caylor (1991) used an interpolation method based on fast Fourier transforms (FFTs) of power samples; their time series data were based on a dwell time of 210 ms. Here we apply a frequency domain procedure (Oppenheim et al. 1983)

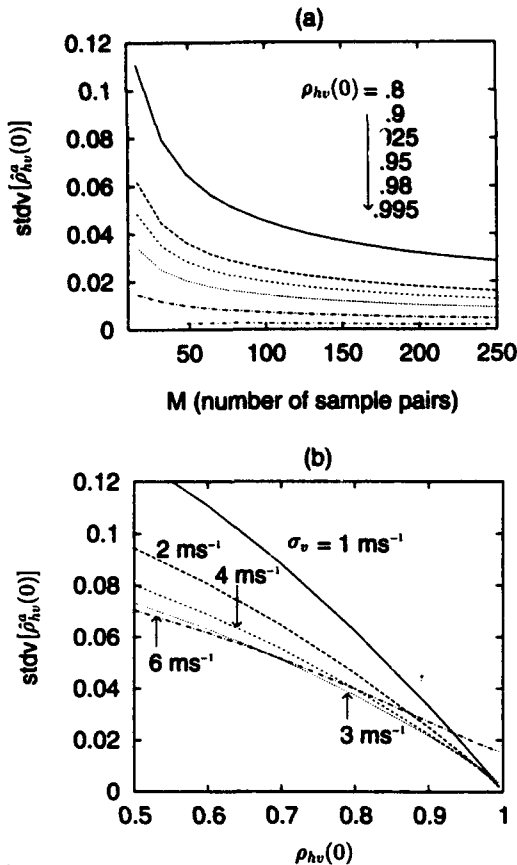


FIG. 2. Theoretically approximated standard deviation (stdv) of  $\hat{\rho}_{hv}(0)$  vs (a) number of sample pairs  $M$ , with  $\sigma_v = 3 \text{ m s}^{-1}$  and  $\rho_{hv}(0)$  as a parameter; (b) true mean  $\rho_{hv}(0)$ , with  $M = 128$  and  $\sigma_v$  as a parameter.

to the alternate complex samples by first substituting zeroes for the missing samples in Fig. 1 and then taking the Fourier transform of the newly formed  $H'/V'$  time series samples followed by ideal low-pass filtering and subsequent inverse Fourier transform to get the interpolated  $H''/V''$  time series samples (see Fig. 4a). The frequency domain procedure yields a correlation coefficient defined as

$$\hat{\rho}_{hv}^F(0) = \frac{(1/2M) \sum_{i=1}^{2M} H_i V_i^*}{(\hat{\rho}_h \hat{\rho}_v)^{0.5}}, \quad (11)$$

where  $\hat{\rho}_h$  and  $\hat{\rho}_v$  are sample mean powers.

The estimators  $\hat{\rho}_{hv}^a(0)$ ,  $\hat{\rho}_{hv}^p(0)$ , and  $\hat{\rho}_{hv}^F(0)$  can be calculated using data from conventional  $Z_{DR}$  radars. It is perhaps obvious that simultaneous measurements of H and V samples is to be preferred for estimating  $\rho_{hv}(0)$ . Sachidananda and Zrnić (1985) consider a radar model that involves simultaneous sampling of the horizontal and vertical polarized received signals from two receivers when the transmit polarization is alternately switched between  $+45^\circ$  and  $-45^\circ$  linear states.

They used this radar model to derive the variance of  $Z_{DR}$  and compare it with the alternate sampling scheme. Jameson and Dave (1988) used circular polarization radar data to estimate  $\rho_{hv}(0)$ , which they term  $\rho_L$ . Figure 4b shows a schematic of the received complex samples for the simultaneous sampling case. For a given dwell time, this method will give  $2M$  sample pairs, whereas the *alternate* method gives  $M$  sample pairs. The copolar correlation coefficient based on simultaneous samples is also given by (11) and is termed  $\hat{\rho}_{hv}^i(0)$ .

The four estimators  $\hat{\rho}_{hv}^a(0)$ ,  $\hat{\rho}_{hv}^p(0)$ ,  $\hat{\rho}_{hv}^F(0)$ , and  $\hat{\rho}_{hv}^i(0)$  are compared in Fig. 5 using the simulation procedure. Both bias and standard deviation are compared versus  $M$  assuming true  $\rho_{hv}(0) = 0.98$ , Gaussian spectrum width  $\sigma_v = 3 \text{ m s}^{-1}$ , and Nyquist velocity  $\lambda/4T_s = 26.75 \text{ m s}^{-1}$ . The magnitude of the bias in  $\hat{\rho}_{hv}^F(0)$  is larger than the other estimators. The standard deviation curves show that  $\hat{\rho}_{hv}^i(0)$  is the best as expected, followed by  $\hat{\rho}_{hv}^F(0)$ ,  $\hat{\rho}_{hv}^a(0)$ , and  $\hat{\rho}_{hv}^p(0)$ . For conventional coherent  $Z_{DR}$  radars,  $\hat{\rho}_{hv}^a(0)$  is ideal for Gaussian spectral shapes as far as minimizing both bias and standard deviation are concerned. Computation

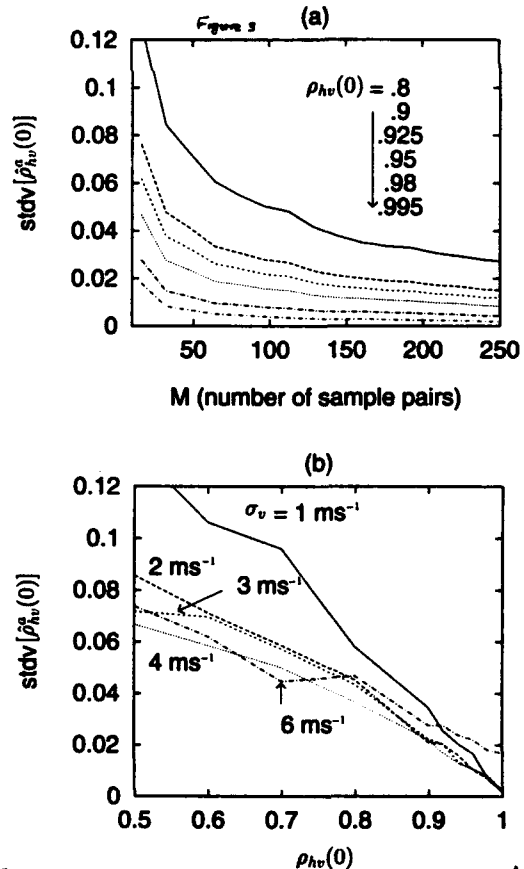


FIG. 3. Simulated standard deviation (stdv) of  $\hat{\rho}_{hv}(0)$  vs (a) number of sample pairs  $M$ , with  $\sigma_v = 3 \text{ m s}^{-1}$  and  $\rho_{hv}(0)$  as a parameter; (b) true mean  $\rho_{hv}(0)$ , with  $M = 128$  and  $\sigma_v$  as a parameter.

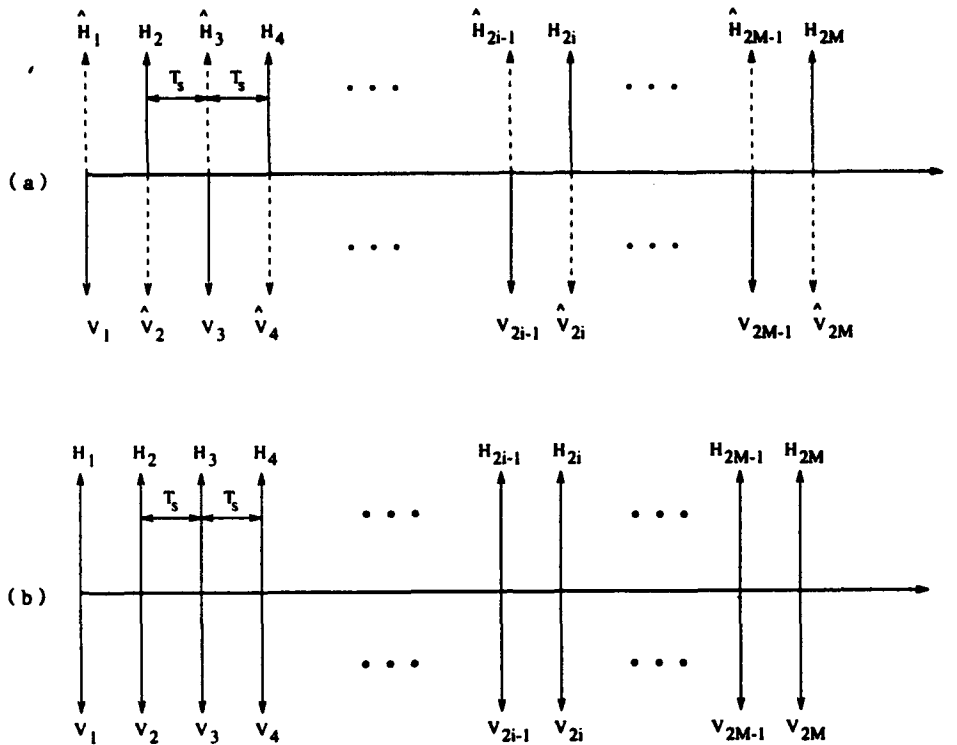


FIG. 4. (a) Interpolation of missing points (dashed lines) of alternate copolar sample sequences; (b) simultaneous copolar complex time sequence (H—horizontal; V—vertical).

over a range of true  $\rho_{hv}(0)$  and  $\sigma_\phi$  show that accuracies of  $\pm 0.01$  can be achieved with  $M > 50$  using  $\hat{\rho}_{hv}^q(0)$ .

2) EFFECTS OF ADDITIVE NOISE

Bringi et al. (1983) derived a simple expression for the effective copolar correlation coefficient  $\rho_{hv}^*(0)$  in the presence of low SNR. They found that, for simultaneous sampling,

$$\rho_{hv}^*(0) = \rho_{hv}(0) \left[ \left( 1 + \frac{1}{\text{SNR}} \right) \left( 1 + \frac{Z_{DR}}{\text{SNR}} \right) \right]^{-1/2} \quad (12)$$

where both SNR and  $Z_{DR}$  are in linear units. The above expression was verified by Illingworth and Caylor (1991) using stratiform rainfall data over a long-range interval (to get different SNR). It is not difficult to derive the expression for the effective  $\rho_{hv}^*(0)$  in the presence of noise for alternate sampling, which is given by

$$\rho_{hv}^{q*}(0) = \rho_{hv}^q(0) \left( 1 + \frac{1}{\text{SNR}} \right)^{-1/4} \left( 1 + \frac{Z_{DR}}{\text{SNR}} \right)^{-1/2} \quad (13)$$

Figure 6 shows the results of simulations for the alternate estimator where the bias in  $\hat{\rho}_{hv}^q(0)$  is plotted versus SNR on a decibel scale. The solid line shows the results of correction based on (13) with  $Z_{DR} = 0$  dB. The fixed

parameters are  $\rho_{hv}(0) = 0.98$ ,  $\sigma_\phi = 3 \text{ m s}^{-1}$ , and  $M = 128$ . It is seen that the correction reduces the bias significantly. However, to keep the bias within  $\pm 0.01$  for the parameters considered in Fig. 6, the SNR should be greater than or equal to 20 dB. Figure 6b shows the results of the corresponding standard deviation versus SNR for the effective  $\hat{\rho}_{hv}^q(0)$  and bias-corrected  $\hat{\rho}_{hv}^{q*}(0)$ . Again, for good accuracy the SNR should exceed 20 dB.

3) EFFECTS OF PHASE NOISE

The pulse-to-pulse rms phase error  $\sigma_\phi$  of the complex signal limits the clutter suppression that is possible in conventional, single-polarized Doppler radar systems (Keeler and Passarelli 1990). Klystron based transmitters can achieve better than  $0.5^\circ$  rms phase error, while coherent-on-receive magnetron systems typically have  $5^\circ$ – $10^\circ$  of rms phase error. A well-designed magnetron system can achieve lower phase errors around  $2^\circ$ – $3^\circ$ .

The simulation method offers a convenient way to handle phase noise. A random phase of zero mean Gaussian  $(0, \sigma_\phi^2)$  was added to the simulated phase of the complex signal  $H_{2i}$  and  $V_{2i+1}$  in Fig. 1. Figure 7a shows the simulation results for the bias in  $\hat{\rho}_{hv}^q(0)$  versus  $\sigma_\phi$  with  $\rho_{hv}(0) = 0.99$ ,  $M = 128$ ,  $\lambda = 5.5 \text{ cm}$ , and  $T_s = 0.83 \text{ m s}^{-1}$ . The magnitude of the bias increases

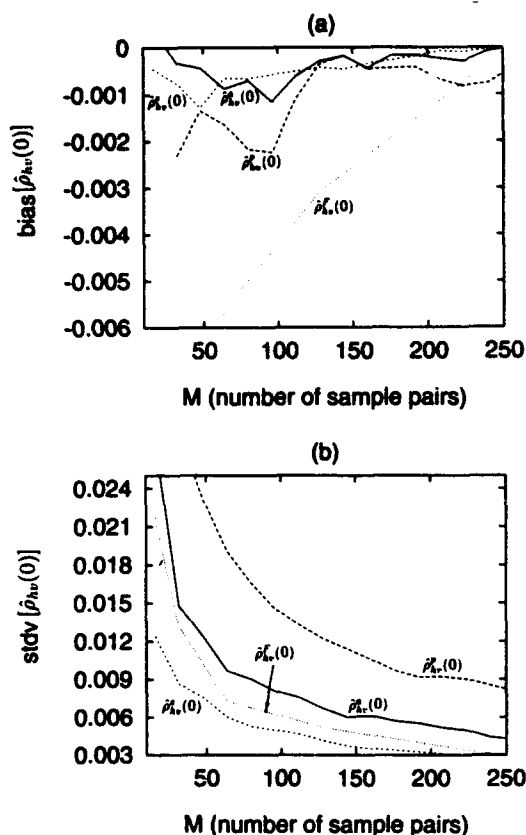


FIG. 5. Simulated (a) bias and (b) standard deviation (stdv) of  $\hat{\rho}_{hv}(0)$  based on estimators  $\hat{\rho}_{hv}^a(0)$ ,  $\hat{\rho}_{hv}^b(0)$ ,  $\hat{\rho}_{hv}^c(0)$ , and  $\hat{\rho}_{hv}^d(0)$  vs number of sample pairs  $M$ , with  $\rho_{hv}(0) = 0.98$ ,  $\sigma_v = 3 \text{ m s}^{-1}$ , and  $\lambda/4T_s = 26.75 \text{ m s}^{-1}$ .

dramatically for  $\sigma_\phi \geq 4^\circ$ . If the bias is to be within 0.01 for the given parameters then  $\sigma_\phi \leq 7^\circ$ . It is obvious that the bias in the power estimator will be independent of  $\sigma_\phi$  and is about 0.001 for the same parameters. Thus, depending on  $M$ ,  $\rho_{hv}(0)$ , and  $\sigma_v$ , there will be a critical value of  $\sigma_\phi$  beyond which the power estimator is preferred. This initial  $\sigma_\phi$  for the parameters used in Fig. 7a is around  $3^\circ$ . Figure 7b shows the corresponding standard deviation of  $\hat{\rho}_{hv}^a(0)$  versus  $\sigma_\phi$  with  $\sigma_v$  as a parameter. Again, the standard deviation increases quite rapidly for  $\sigma_\phi \geq 5^\circ$ . For coherent-on-receive magnetron systems with  $\sigma_\phi > 3^\circ$  it is better to use the power estimator of  $\hat{\rho}_{hv}(0)$  using (10) or the interpolation method used by Illingworth and Caylor (1991). This will avoid serious biases in  $\hat{\rho}_{hv}(0)$ .

#### 4) EFFECTS OF NON-GAUSSIAN SPECTRA

The simulation procedure can also be applied to non-Gaussian spectra, for example, double-peaked spectra. Multiple-peaked spectra can be generated by superimposing different Gaussian spectra, each having different mean velocity  $\bar{v}$ , spectral width  $\sigma_v$ , and/or the

mean power  $P$ . An example of such a simulated power spectrum is shown in Fig. 8 where the Nyquist velocity is  $25 \text{ m s}^{-1}$ . The shape about each peak (at  $\bar{v}_1 = -6 \text{ m s}^{-1}$  and  $\bar{v}_2 = 5 \text{ m s}^{-1}$ ) is Gaussian with  $\sigma_{v_1} = 2 \text{ m s}^{-1}$ ,  $P_1 = 1 \text{ mW}$ , and  $\sigma_{v_2} = 3 \text{ m s}^{-1}$ ,  $P_2 = 2 \text{ mW}$ , respectively.

Figure 9a shows the bias in  $\hat{\rho}_{hv}^a(0)$  (solid and dashed lines) and  $\hat{\rho}_{hv}^b(0)$  (discrete points) as a function of  $M$  for symmetric double-peaked spectra with fixed  $\sigma_{v_1} = \sigma_{v_2} = 3 \text{ m s}^{-1}$  and  $\bar{v}_1 = \bar{v}_2 = \bar{v}$  as a parameter. Because the alternate estimator  $\hat{\rho}_{hv}^a(0)$  is derived for Gaussian spectrum, it is not unexpected to note rather large biases in  $\hat{\rho}_{hv}^a(0)$  for non-Gaussian spectra. Since true  $\rho_{hv}(0)$  was chosen to be 0.98, the estimated values will exceed 1 for  $\bar{v} \geq 5 \text{ m s}^{-1}$ . We emphasize that  $\bar{v}$  is not the mean velocity calculated for the entire spectrum, rather it is the center of one of the Gaussian shapes shown in Fig. 8. Note also the tendency for the bias to increase with  $M$  for  $\bar{v} = 6 \text{ m s}^{-1}$ . It is clear that the bias is serious and  $\hat{\rho}_{hv}^a(0)$  should not be used for non-Gaussian spectra. In contrast, the bias in  $\hat{\rho}_{hv}^b(0)$  decreases with  $M$ . Figure 9b shows the standard error of  $\hat{\rho}_{hv}^a(0)$  for  $\bar{v} = 0$ ,

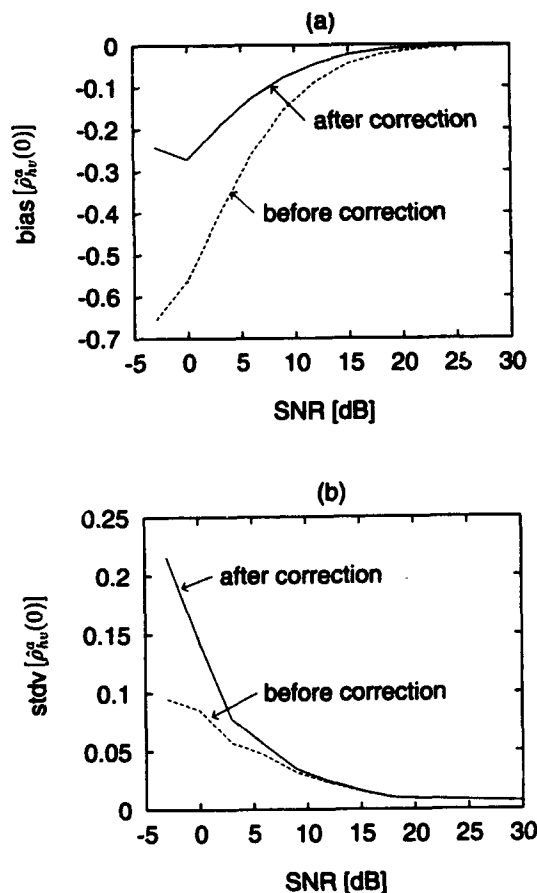


FIG. 6. Simulated (a) bias and (b) standard deviation (stdv) of  $\hat{\rho}_{hv}^a(0)$  versus signal-to-noise ratio (SNR) before and after the noise correction using (12), with  $\rho_{hv}(0) = 0.98$ ,  $\sigma_v = 3 \text{ m s}^{-1}$ , and  $M = 128$ .

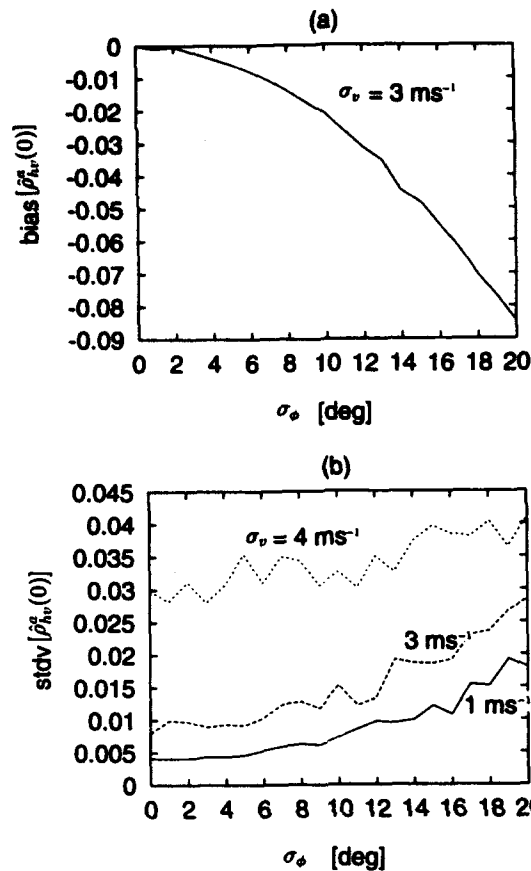


FIG. 7. Simulated (a) bias and (b) standard deviation (stdv) of  $\hat{\rho}_{hv}^a(0)$  vs rms phase error  $\sigma_\phi$ , with  $\rho_{hv}(0) = 0.98$ ,  $M = 128$ , and  $\sigma_v$  as parameter.

5, and 6  $m s^{-1}$ . Also shown is the standard error of  $\hat{\rho}_{hv}^F(0)$  for  $\bar{v} = 6 m s^{-1}$  (the curves for 0 and 5  $m s^{-1}$  are very near the  $\bar{v} = 6 m s^{-1}$  curve but lower and hence not shown). By comparing the bias and standard error in  $\hat{\rho}_{hv}^a(0)$  and  $\hat{\rho}_{hv}^F(0)$  for non-Gaussian spectral shapes, it is clear that  $\hat{\rho}_{hv}^F(0)$  is preferred.

### 3. Radar time series analysis

The CSU CHILL radar is an S-band, dual linear-polarized Doppler radar that can be operated in a time series mode that allows recording of the complex  $I, Q$  signals for every pulse at 40 range resolution volumes, which permits an analysis of signal fluctuations. The radar and signal processor are described by Mueller and Staggs (1986) and Brunkow and Lee (1986). Recently, the signal processor was programmed to compute and display  $\hat{\rho}_{hv}^a(0)$  in real time.

On 25 June 1992 time series data were collected for several minutes with the antenna stationary and pointing at a convective precipitation shaft at an elevation angle of  $2^\circ$  and in the range interval 60–70 km (altitude approximately 2.3 km AGL, near the melting level).

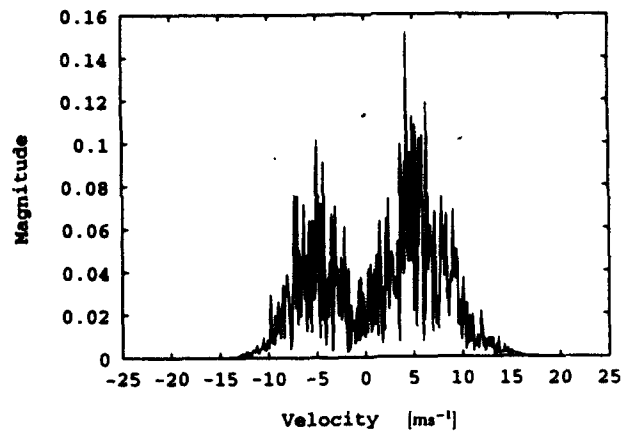


FIG. 8. Simulated spectrum magnitude (128-point periodogram) with two peaks centered at  $\bar{v}_1 = -6 m s^{-1}$  and  $\bar{v}_2 = 5 m s^{-1}$ . The shape about each peak is Gaussian with  $\sigma_{\omega 1} = 2 m s^{-1}$ ,  $P_1 = 1 mW$ , and  $\sigma_{\omega 2} = 3 m s^{-1}$ ,  $P_2 = 2 mW$ , respectively.

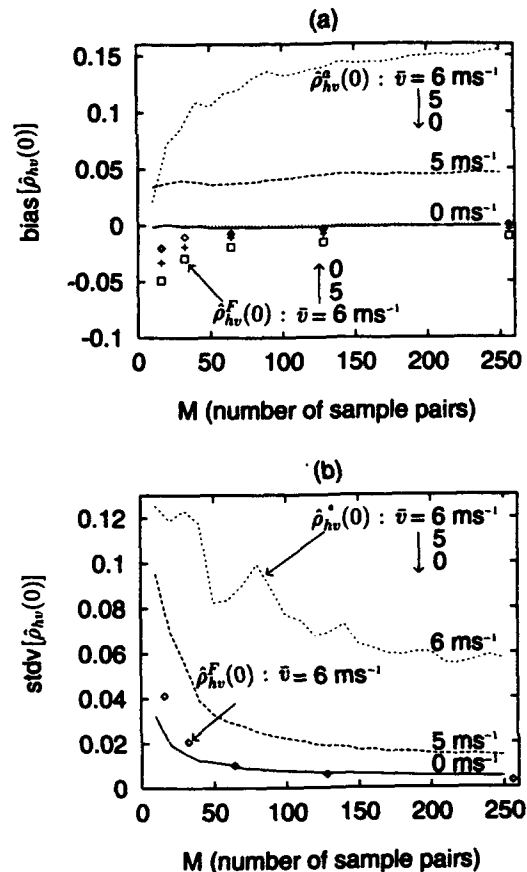


FIG. 9. Comparison between  $\hat{\rho}_{hv}^a(0)$  and  $\hat{\rho}_{hv}^F(0)$  for Gaussian spectrum ( $\bar{v} = 0$ ) and double-peak spectrum ( $\bar{v}_1 = \bar{v}_2 = 5, 6 m s^{-1}$ , respectively). Simulated (a) bias and (b) standard deviation (stdv) of  $\hat{\rho}_{hv}(0)$  vs number of sample pairs  $M$ , with  $\rho_{hv}(0) = 0.98$  and  $\sigma_v = 3 m s^{-1}$ .

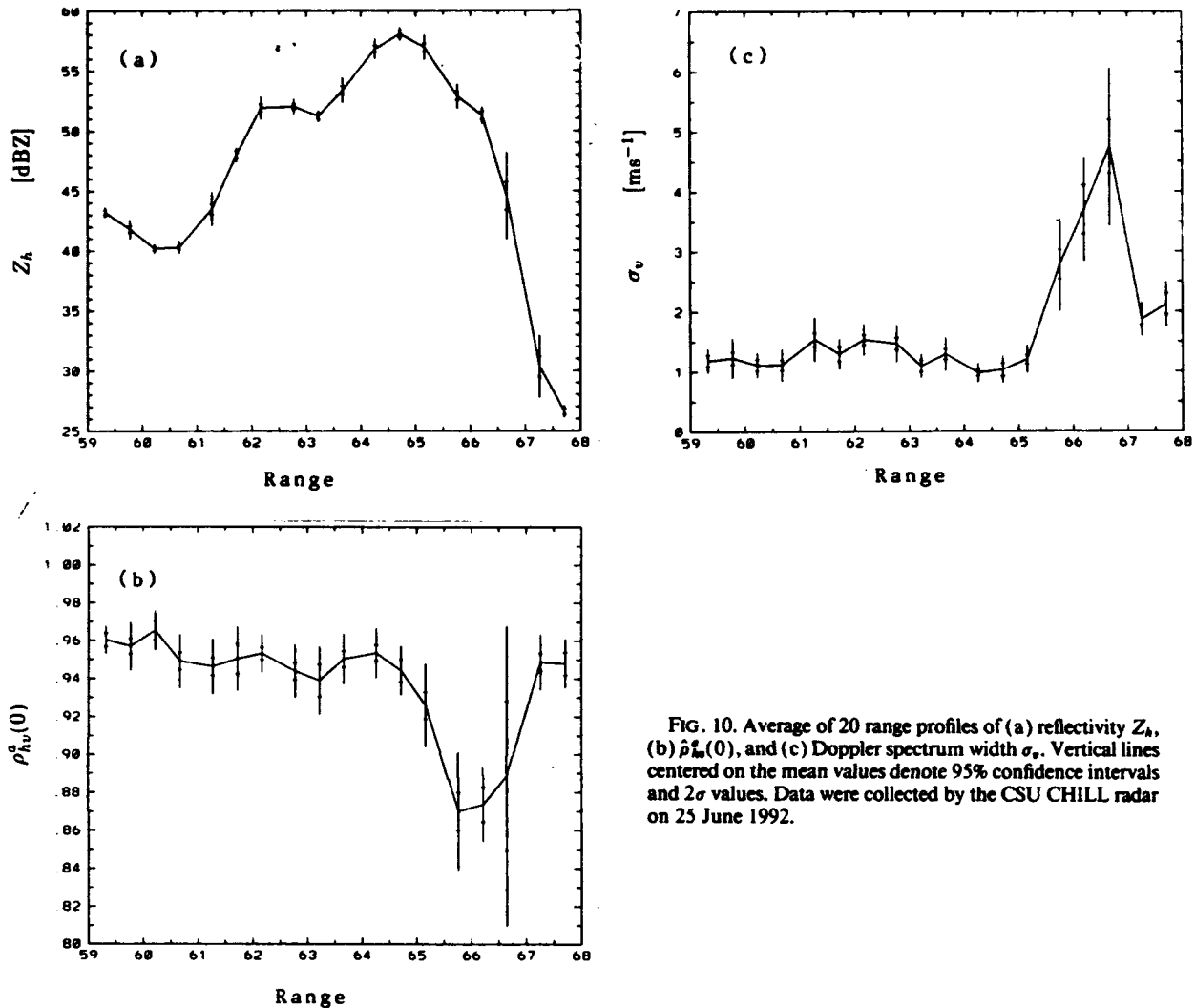


FIG. 10. Average of 20 range profiles of (a) reflectivity  $Z_h$ , (b)  $\hat{\rho}_{hv}^a(0)$ , and (c) Doppler spectrum width  $\sigma_v$ . Vertical lines centered on the mean values denote 95% confidence intervals and  $2\sigma$  values. Data were collected by the CSU CHILL radar on 25 June 1992.

Figure 10 shows range profiles of (a) reflectivity  $Z_h$ , (b)  $\hat{\rho}_{hv}^a(0)$ , and (c) Doppler spectrum width  $\sigma_v$ . The average of 20 range profiles (6 s of data) is shown together with 95% confidence interval and  $2\sigma$  standard error bars for each variable. The main precipitation core (peak  $Z_h \sim 59$  dBZ) is clearly visible at a range of 64.5 km. The main feature in  $\hat{\rho}_{hv}^a(0)$  is a region of lowered values between 65 and 67 km and the very large  $2\sigma$  value (0.16) at 66.6 km. In this same region the Doppler spectral width is significantly enhanced (peak of  $4.5$   $\text{m s}^{-1}$ ) with  $2\sigma$  value of  $2.15$   $\text{m s}^{-1}$  at 66.7 km. The mean velocity (not shown here) changes quite sharply from  $-2.5$   $\text{m s}^{-1}$  at 65 km to about  $0.5$   $\text{m s}^{-1}$  at 67 km, indicative of radial divergence near the melting level. The intention in this paper is not to provide a microphysical explanation for the data, rather our interest is in the properties of the  $\hat{\rho}_{hv}^a(0)$  estimator. Three resolution volumes centered at 62.3, 65.7, and 66.7 km were chosen for analysis, the corresponding

mean  $Z_h$ ,  $\hat{\rho}_{hv}^a(0)$ , and  $\sigma_v$  being, respectively, 52 dBZ, 0.95,  $1.5$   $\text{m s}^{-1}$ ; 53 dBZ, 0.87,  $2.75$   $\text{m s}^{-1}$ ; and 45 dBZ, 0.89,  $4.3$   $\text{m s}^{-1}$ . The Doppler spectrum shapes at the resolution volume at 62.3, 65.7, and 66.7 km were modeled based on the measured spectra and are shown in Fig. 11. The shapes are characterized as (a) narrow, (b) double-peak, and (c) wide. Using these modeled spectra and true  $\rho_{hv}(0)$  of 0.95 for (a), 0.87 for (b), and 0.89 for (c), the standard deviations of  $Z_{DR}$ ,  $\Phi_{DP}$ , and  $\hat{\rho}_{hv}^a(0)$  were calculated versus  $M$  using the simulation method with  $\lambda/4T_r = 26.75$   $\text{m s}^{-1}$ . The results are shown in Fig. 12 together with the experimentally measured standard deviations. The agreement between measurements and simulations is quite good as far as standard errors are concerned. The effect of Doppler spectral shape, while not affecting standard errors in  $Z_{DR}$  and  $\Phi_{DP}$ , is quite pronounced in Fig. 12c, which shows the standard error in  $\hat{\rho}_{hv}^a(0)$ . Figure 13 compares the standard errors in the three estimators

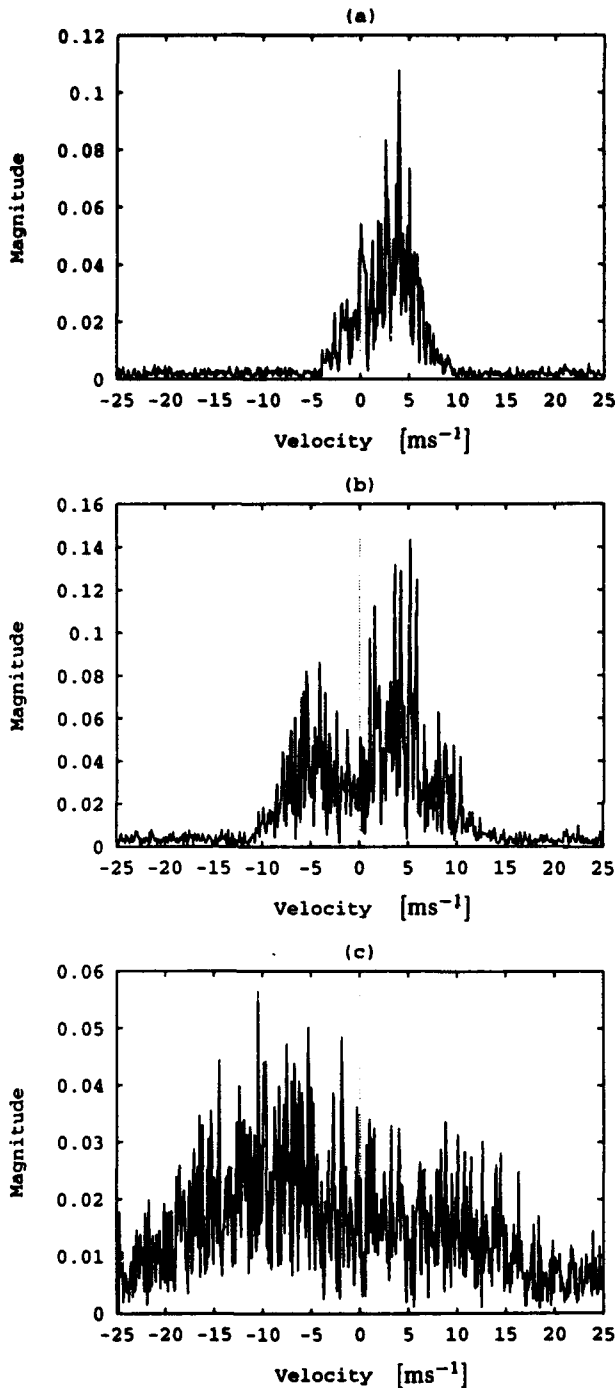


FIG. 11. Modeled spectra based on radar data time series measurements taken on 25 June 1992: (a) narrow, (b) double peak, and (c) wide.

$\hat{\rho}_{hv}^q(0)$ ,  $\hat{\rho}_{hv}^p(0)$ , and  $\hat{\rho}_{hv}^f(0)$  as a function of  $M$  using the measured time series data for (a) narrow, (b) double-peak, and (c) wide spectral shapes. While the agreement between  $\hat{\rho}_{hv}^q(0)$  and  $\hat{\rho}_{hv}^f(0)$  is very good for (a) and (b), case (c) shows that  $\hat{\rho}_{hv}^f(0)$  is the preferred

estimator for wide spectral shapes. Finally, Fig. 14 shows the mean  $\hat{\rho}_{hv}(0)$  versus  $M$  for the three estimators based on measured time series data for (a) narrow, (b) double-peak, and (c) wide spectral shapes.

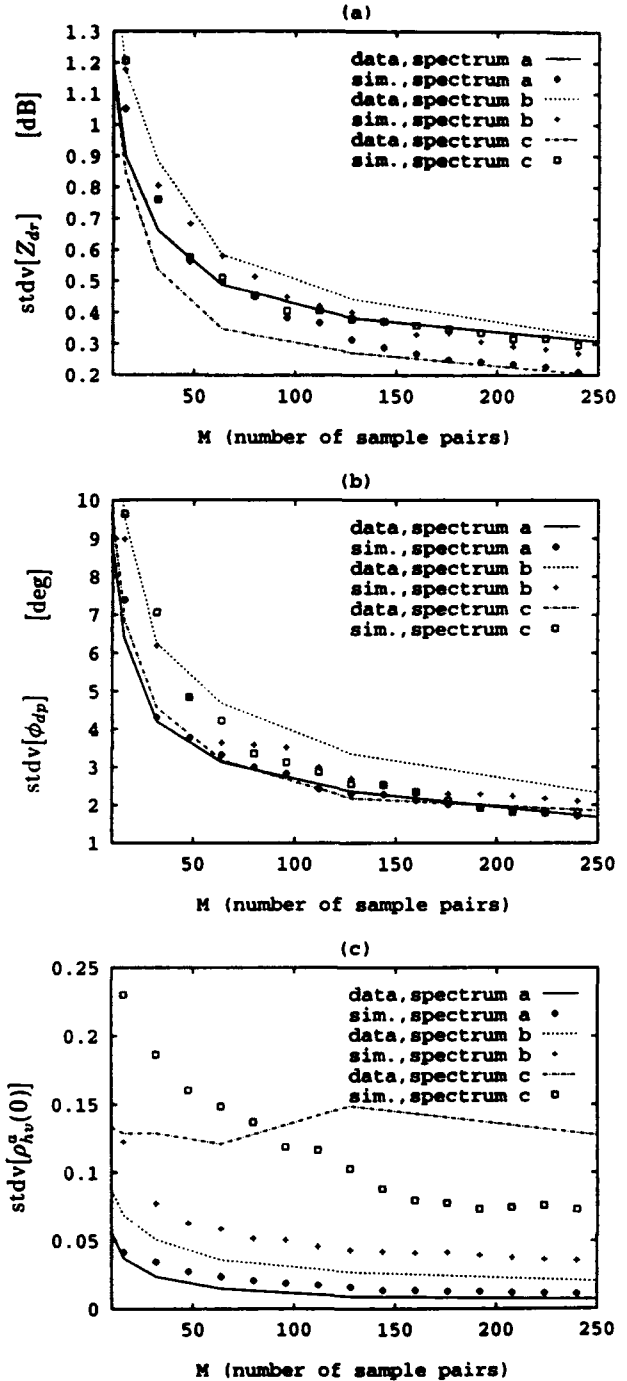


FIG. 12. Standard deviation (stdv) of (a)  $Z_{DR}$ , (b)  $\hat{\phi}_{DP}$ , and (c)  $\hat{\rho}_{hv}^q(0)$  vs number of sample pairs  $M$  based on data, collected by CSU CHILL radar, and simulations corresponding to the spectrum of Figs. 11a, 11b, and 11c respectively.

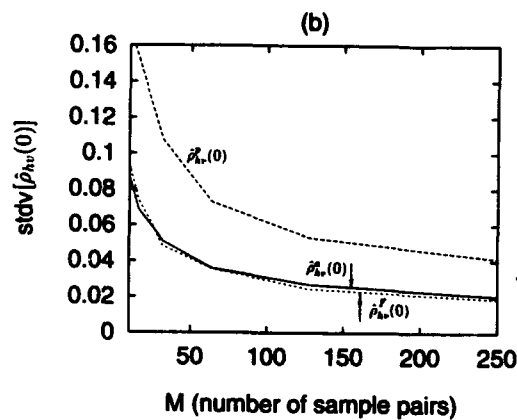
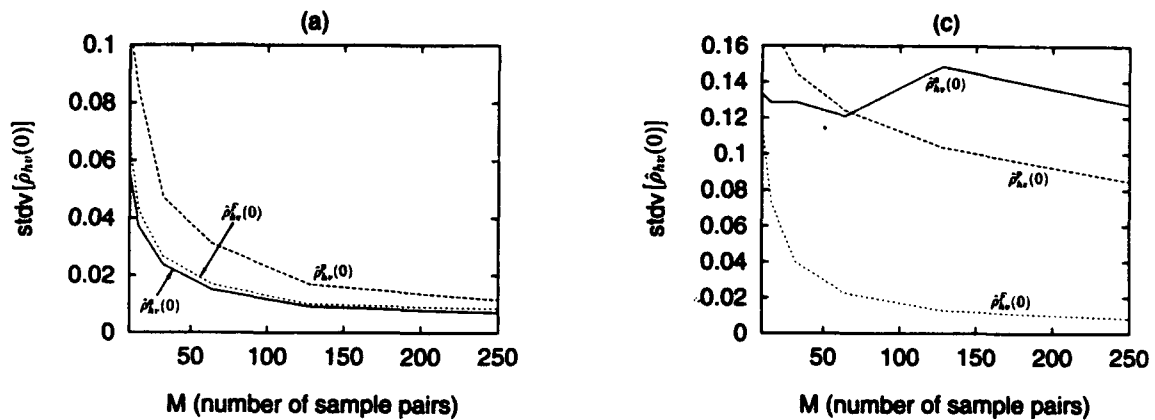


FIG. 13. (a), (b), and (c) Standard deviation (stdv) of  $\hat{\rho}_{hv}(0)$  vs number of sample pairs  $M$  based on CSU CHILL radar data corresponding to the spectrum of Figs. 11a, 11b, and 11c, respectively, for  $\hat{\rho}_{hv}^f(0)$ ,  $\hat{\rho}_{hv}^g(0)$ , and  $\hat{\rho}_{hv}^h(0)$ .

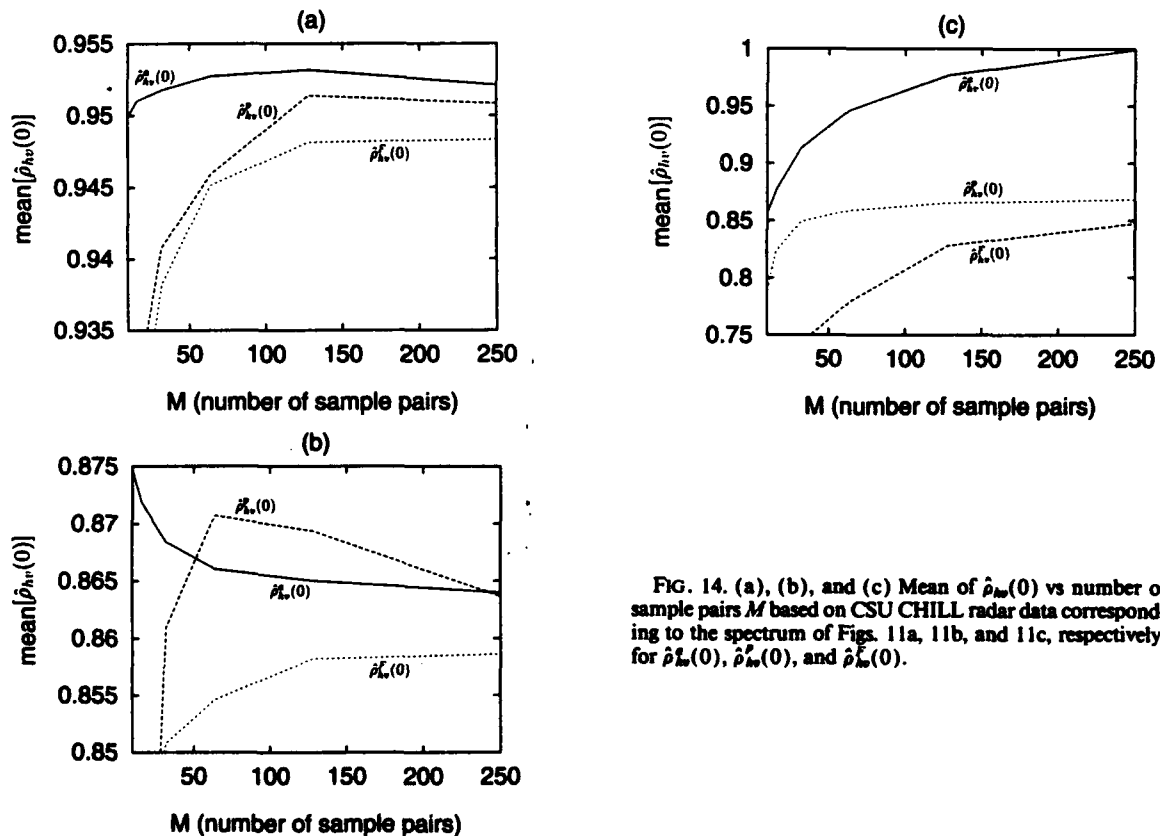


FIG. 14. (a), (b), and (c) Mean of  $\hat{\rho}_{hv}(0)$  vs number of sample pairs  $M$  based on CSU CHILL radar data corresponding to the spectrum of Figs. 11a, 11b, and 11c, respectively, for  $\hat{\rho}_{hv}^f(0)$ ,  $\hat{\rho}_{hv}^g(0)$ , and  $\hat{\rho}_{hv}^h(0)$ .

While good convergence is obtained experimentally for cases (a) and (b), case (c) shows that mean  $\hat{\rho}_{hv}^q(0)$  does not converge as a function of  $M$  and can exceed unity; thus, again  $\hat{\rho}_{hv}^F(0)$  is the preferred estimator in agreement with the simulation results for non-Gaussian spectral shapes discussed in section 2b.

#### 4. Antenna pattern effects

The previous discussion of the accuracy of  $\hat{\rho}_{hv}(0)$  implicitly assumes an ideal antenna. However, real antennas are not ideal and, in particular, phase matching (and to a lesser extent amplitude matching) of the horizontal and vertical polarized patterns within the main lobe is crucial for accurate  $\hat{\rho}_{hv}(0)$  measurements. The antenna differential phase  $\Phi_{DA}$  is defined as  $\phi_h - \phi_v$ , where  $\phi_h$  and  $\phi_v$  are the phase patterns. Normally, a precise reflector illuminated by a well-designed, dual-polarized horn will achieve a nearly constant  $\Phi_{DA}$  within the main lobe. The  $\Phi_{DA}$  pattern of the CSU CHILL radar was measured and it showed a rather significant change over the main lobe (Xiao et al. 1993). The antenna thus sets an upper bound on the measured  $\hat{\rho}_{hv}(0)$ . If  $\rho_A$  is the antenna coefficient, it is given (neglecting second order cross-polar errors) by

$$\rho_A = \frac{\left| \int f_h f_v e^{j2\Phi_{DA}} d\Omega \right|}{\left( \int f_h^2 d\Omega \int f_v^2 d\Omega \right)^{1/2}}, \quad (14)$$

where  $f_h$  and  $f_v$  are the conventional copolar power patterns. A two-dimensional integration ( $5^\circ \times 5^\circ$  sector around boresight) of the measured patterns yielded  $\hat{\rho}_A = 0.99$ , which is the upper limit on the observed  $\rho_{hv}(0)$ . In the case of the CSU CHILL antenna we believe that numerous teardowns and reassemblies of the reflector has caused a deterioration in the reflector accuracy. In contrast, the measurements reported by Illingworth and Caylor (1991) in very light rainfall show the upper limit of their antenna to be 0.998. Both the National Severe Storm Laboratory Cimarron and National Center for Atmospheric Research CP-2 radars appear to have the upper limit of  $\rho_{hv}(0)$  limited by the antenna to 0.985–0.990 (Balakrishnan and Zrnić 1990; Liu et al. 1993).

#### 5. Conclusions

This study was motivated by the findings of Illingworth and Caylor (1991), who found that the standard deviation of  $\hat{\rho}_{hv}(0)$  obtained from time series data did not agree with (was much smaller than) the theoretical predictions of Balakrishnan and Zrnić (1990). We have derived the standard deviation and bias of  $\hat{\rho}_{hv}(0)$  for the *alternate* estimator using the perturbation approach described by Balakrishnan and Zrnić (1990). We also used the simulation procedure of Chandrasekar et al.

(1986) to compare with the perturbation approach and found good agreement. Our results also agree well with the experimental results of Illingworth and Caylor (1991). A number of other estimators of  $\rho_{hv}(0)$  were analyzed using simulations, that is, those based on power samples, simultaneous samples of H and V returns, and an FFT-based interpolation method used to approximate simultaneous sampling. For Gaussian spectrum, the alternate sample-based estimator of  $\rho_{hv}(0)$  gives smaller standard deviations and bias compared with the power and FFT estimators. For non-Gaussian spectrum, the FFT method is significantly better than the alternate and power methods both of which give unacceptably large bias. Other factors that introduce bias are low SNR and high phase noise. Large bias can be introduced by low SNR for all estimators when SNR < 20 dB. Simulations show that when the rms phase noise exceeds about  $5^\circ$  (e.g., magnetron-based systems) the power estimator of  $\rho_{hv}(0)$  should be used to avoid rather large biases that occur when using the alternate method based on complex samples. A bias in  $\rho_{hv}(0)$  can also be caused by the antenna if the phase difference pattern between H and V polarizations is not uniform across the main beam. Amplitude matching of the copolar patterns, while important for accurate  $Z_{DR}$  measurements, is not so critical for  $\rho_{hv}(0)$ . This depends on feedhorn imperfections and/or reflector inaccuracy. Thus it is exceedingly difficult to achieve an accuracy level of  $\pm 0.001$  in  $\rho_{hv}(0)$  because of these various factors. The best results so far have been reported by Illingworth and Caylor (1991), who used a dwell time of 210 ms in conditions likely to be dominated by narrow spectral widths and Gaussian shapes. Even then they inferred a residual bias of  $-0.002$  in order to bring their  $\rho_{hv}(0)$  versus  $Z_{DR}$  data in better agreement with a gamma drop size distribution model with varying  $m$  parameter. The reduced accuracy of  $\pm 0.01$  which is sufficient for hail detection is readily attainable by using  $\hat{\rho}_{hv}^q(0)$  if the spectral shape is Gaussian and by using  $\hat{\rho}_{hv}^F(0)$  for shapes deviating substantially from Gaussian. To achieve very high accuracies in  $\rho_{hv}(0)$  under all conditions, simultaneous sampling is the only alternative at the cost of increased system complexity.

*Acknowledgments.* This research was supported by National Science Foundation Grant ATM-9014600 and AFOSR Grant 91-0141. The CSU CHILL radar is sponsored by NSF Grant ATM-8919080.

#### REFERENCES

- Balakrishnan, N., and D. S. Zrnić, 1990: Use of polarization to characterize precipitation and discriminate large hail. *J. Atmos. Sci.*, 47, 1525–1540.
- Bringi, V. N., T. A. Seliga, and S. M. Cherry, 1983: Statistical properties of the dual-polarization differential reflectivity ( $Z_{DR}$ ) radar signal. *IEEE Trans. Geosci. Remote Sens.*, 21, 215–220.
- , V. Chandrasekar, N. Balakrishnan, and D. S. Zrnić, 1990: An examination of propagation effects in rainfall on radar mea-

- surements at microwave frequencies. *J. Atmos. Ocean. Technol.*, 7, 829-840.
- Brunkow, D. A., and R. Lee, 1986: CHILL data system. Preprints, *23d Radar Meteorology Conf.*, Snowmass, CO, Amer. Meteor. Soc., JP354-JP356.
- Chandrasekar, V., and V. N. Bringi, 1988: Error structure of multiparameter radar and surface measurements of rainfall. Part I: Differential reflectivity. *J. Atmos. Oceanic Technol.*, 5, 783-795.
- , V. N. Bringi, and P. J. Brockwell, 1986: Statistical properties of dual-polarized radar signals. Preprints, *23d Radar Meteorology Conf.*, Snowmass, CO, Amer. Meteor. Soc., 193-196.
- , V. N. Bringi, N. Balakrishnan, and D. S. Zrnić, 1990: Error structure of multiparameter radar and surface measurements of rainfall. Part III: Specific differential phase. *J. Atmos. Oceanic Technol.*, 7, 621-629.
- , J. Hubbert, and V. N. Bringi, 1993: Transformation of dual polarized radar data via the instantaneous scattering matrix. *26th Int. Conf. on Radar Meteorology*, Norman, OK, Amer. Meteor. Soc., 118-120.
- Doviak, R. J., and D. S. Zrnić, 1984: *Doppler Radar and Weather Observations*. Academic Press, 458 pp.
- Green, J. W., 1990: Simulation of multivariate radar signals. M.S. thesis, The University of Alabama, Huntsville, 152 pp.
- Illingworth, J. A., and I. J. Caylor, 1991: Co-polar correlation measurements of precipitation. Preprints, *25th Conf. on Radar Meteorology*, Paris, Amer. Meteor. Soc., 650-653.
- Jameson, A. R., 1989: The interpretation and meteorological application of radar backscatter amplitude ratios at linear polarizations. *J. Atmos. Ocean. Technol.*, 6, 908-919.
- , and J. H. Dave, 1988: An interpretation of circular polarization measurements affected by propagation differential phase shift. *J. Atmos. Oceanic Technol.*, 5, 405-415.
- Keeler, R. J., and R. E. Passarelli, 1990: Signal processing for atmospheric radars. *Radar in Meteorology*, D. Atlas, Ed., Amer. Meteor. Soc., 199-229.
- Liu, L., V. N. Bringi, I. J. Caylor, and V. Chandrasekar, 1993: Intercomparison of multiparameter radar signatures from Florida storms. *26th Int. Conf. on Radar Meteorology*, Norman, OK, Amer. Meteor. Soc., 733-735.
- Mueller, E. A., and D. W. Staggs, 1986: Capabilities of the CHILL radar after update. Preprints, *23d Radar Meteorology Conf.*, Snowmass, CO, Amer. Meteor. Soc., JP352-JP353.
- Oppenheim, A. V., A. S. Willsky, and I. T. Young, 1983: Signals and systems. *Prentice-Hall*, 769 pp.
- Sachidananda, M., and D. S. Zrnić, 1985:  $Z_{DR}$  measurement considerations for a fast scan capability radar. *Radio Sci.*, 20, 907-922.
- , and —, 1989: Efficient processing of alternately polarized radar signals. *J. Atmos. Oceanic Technol.*, 6, 235-247.
- Xiao, R., V. N. Bringi, D. Garbrick, E. A. Mueller, and S. A. Rutledge, 1993: Copolar and cross-polar pattern measurements of the CSU-CHILL antenna. *26th Int. Conf. on Radar Meteorology*, Norman, OK, Amer. Meteor. Soc., 363-365.
- Zrnić, D. S., 1977: Spectral moment estimates from correlated pulse pairs. *IEEE Trans. Aerosp. Electron. Syst.*, 13, 344-354.
- , V. N. Bringi, N. Balakrishnan, K. Aydin, V. Chandrasekar, and J. Hubbert, 1993: Polarimetric measurements in a severe hailstorm. *Mon. Wea. Rev.*, 121, 2223-2238.

# STATISTICAL CHARACTERISTICS OF THE COPOLAR CORRELATION COEFFICIENT BETWEEN HORIZONTAL AND VERTICAL POLARIZATIONS

L. Liu, V.N. Bringi, V. Chandrasekar, E.A. Mueller and A. Mudukutore  
Colorado State University, Fort Collins, CO 80523

## 1. INTRODUCTION

In this paper, we derive the bias and variance of  $\hat{\rho}_{hv}(0)$  using the perturbation method. These results are then compared with simulations. Several different estimators of  $\rho_{hv}(0)$  are considered. Time series data collected with the CSU-CHILL radar are analyzed.

## 2. STATISTICAL ASPECTS

### 2.1. Perturbation Method

By assuming a Gaussian spectrum, the estimator for  $\rho_{hv}(0)$  can be written as (Sachidananda & Zrnic, 1989)

$$\hat{\rho}_{hv}(0) = \hat{\rho}_{hv}(1) / [\hat{\rho}(2)]^{0.25} \quad (1)$$

where

$$\hat{\rho}_{hv}(1) = \frac{|\sum_{i=1}^M H_{2i} V_{2i+1}^*|}{[\sum_{i=1}^M |H_{2i}|^2 \sum_{i=1}^M |V_{2i+1}|^2]^{0.5}}$$

$$\hat{\rho}(2) = \hat{\rho}_{hh}(2) = \frac{|\sum_{i=1}^M H_{2i} H_{2i+2}^*|}{\sum_{i=1}^M |H_{2i}|^2}$$

The method described by Balakrishnan & Zrnic (1990) is used to derive the bias and standard derivation of  $\hat{\rho}_{hv}(0)$  defined in Eq. (1). The expressions for bias and variance of  $\hat{\rho}_{hv}(0)$  are long and will be given later in a journal paper.

Fig.1 shows a schematic of the alternately received copolar time samples,  $\{H_{2i}\}$  and  $\{V_{2i+1}\}$ . Fig.2 shows the predicted standard deviation of  $\hat{\rho}_{hv}(0)$  vs (a) M, and, (b)  $\rho_{hv}(0)$ . In (a)  $\sigma_v = 3 \text{ m/s}$  and  $\rho_{hv}(0)$  is a parameter, while in (b)  $M = 128$  with  $\sigma_v$  as a parameter. Fig.2b shows that the standard deviation decreases more or less linearly with increasing  $\rho_{hv}(0)$ , a fact deduced empirically by Illingworth & Caylor (1991) from their data.

### 2.2. Simulations

We use the simulation method (Chandrasekar et al., 1986) to study the fluctuations in  $\hat{\rho}_{hv}(0)$  and compare it with the perturbation method. It can also be used to study other estimators of  $\rho_{hv}(0)$  and the effects of SNR, phase noise and non-Gaussian spectral shapes on the bias and variance of  $\hat{\rho}_{hv}(0)$ .

Fig.3 shows the standard deviation of  $\hat{\rho}_{hv}(0)$  vs (a) M, and, (b)  $\rho_{hv}(0)$  which can be compared with Fig.2. The related bias is very small (typically  $< 0.001$ ). Excellent agreement is found between the perturbation method and the simulations which gives confidence in applying the simulation method to study other estimators of  $\rho_{hv}(0)$ .

### 2.3. Other Estimators of $\rho_{hv}(0)$

The Estimator defined in Eq. (1) will be termed the alternate sample based estimator or  $\hat{\rho}_{hv}^a(0)$ . For incoherent radars, power samples can be used to estimate  $\rho_{hv}(0)$ .

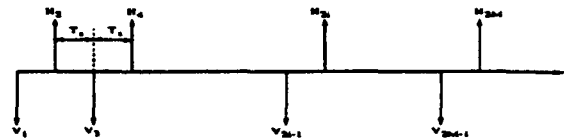


Fig.1 Alternate co-polar complex time sequence. (H - horizontal; v - vertical)

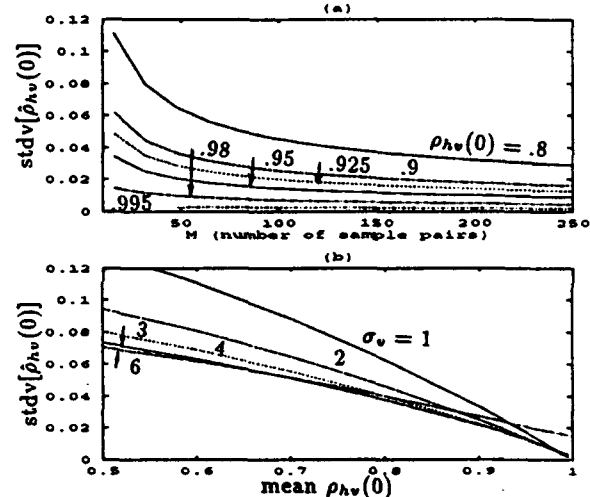


Fig.2 Theoretically approximated  $\text{stdv}[\hat{\rho}_{hv}(0)]$  vs number of sample pairs M, with  $\sigma_v = 3 \text{ m/s}$ ; (a) vs true mean  $\rho_{hv}(0)$ , with  $M = 128$ .

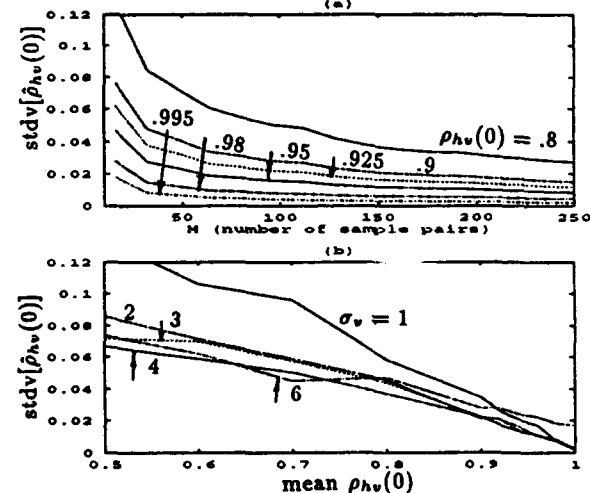


Fig.3 Simulated  $\text{stdv}[\hat{\rho}_{hv}(0)]$  vs number of sample pairs M, with  $\sigma_v = 3 \text{ m/s}$ ; (a) vs true mean  $\rho_{hv}(0)$ , with  $M = 128$ .

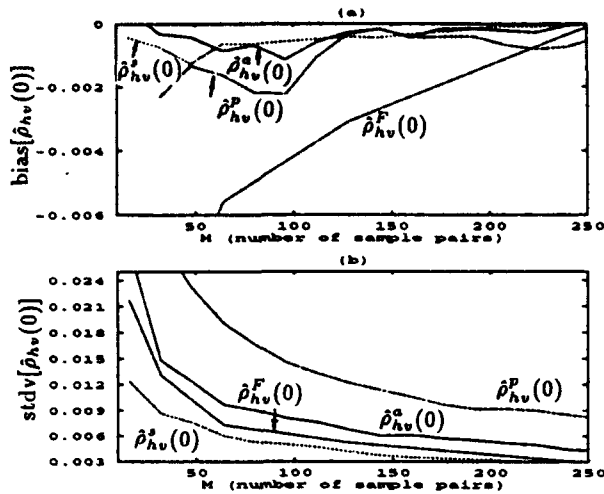


Fig.4 Simulated (a) bias $[\hat{\rho}_{hv}(0)]$  and (b) stdv $[\hat{\rho}_{hv}(0)]$  based on different estimators vs number of sample pairs  $M$ , with  $\rho_{hv}(0) = .98$  and  $\sigma_v = 3m/s$ .

Let  $p_h(2i)$  and  $p_v(2i+1)$  be the alternately received power samples as shown in the schematic of Fig.1. The estimate of the copolar power correlation coefficient  $\hat{\rho}_{p_h, p_v}(0)$  can be written as,

$$\begin{aligned} \hat{\rho}_{p_h, p_v}(0) &= \hat{\rho}_{p_h, p_v}(1) / [\hat{\rho}_{p_h, p_h}(2)]^{0.25} \\ \hat{\rho}_{hv}(0) &= [\hat{\rho}_{p_h, p_v}(0)]^{0.5} \end{aligned} \quad (2)$$

This follows from the fact that  $\rho_p = \rho^2$  where  $\rho_p$  stands for  $\rho_{p_h}$  or  $\rho_{p_v}$  (Doviak & Zrnic, 1984). Estimator defined by Eq. (2) will be termed the power sample based estimate or  $\hat{\rho}_{hv}^p(0)$ .

For the simultaneous sampling case,  $\rho_{hv}(0)$  can be estimated based on  $2M$  pairs of H/V samples for a given dwell time in which alternate method gives  $M$  sample pairs, i.e.,

$$\hat{\rho}_{hv}^s(0) = \frac{1}{2M} \sum_{i=1}^{2M} H_i V_i^* / [\hat{p}_h \hat{p}_v]^{0.5} \quad (3)$$

where  $\hat{p}_h$  and  $\hat{p}_v$  are estimates of mean sample powers. Eq. (3) is termed simultaneous estimator.

In order to approximate the simultaneous sampling case, we apply the FFT technique on the alternate complex sample sequences for interpolation (Oppenheim & Willisky, 1983) to estimate  $\rho_{hv}(0)$  using the Eq. (3), which is termed FFT based estimator or  $\hat{\rho}_{hv}^F(0)$ .

The four estimators for  $\rho_{hv}(0)$  are compared in Fig.4 using simulations. The alternate, simultaneous and FFT estimators are in excellent agreement as far as bias and standard deviation are concerned. The power estimator has a small negative bias even for large  $M$  which is in agreement with Illingworth & Caylor (1991). The standard deviation is somewhat higher for the power estimator as compared to the other three.

### 3. TIME SERIES MEASUREMENT

On 25 June 1992 time series data were collected by the CSU-CHILL radar with the antenna stationary and pointing at a convective precipitation shaft located in the range interval 60 - 70 km. Three resolution volumes centered at 62.3, 65.9 and 66.5 km were chosen for analysis which had widely different Doppler spectra as shown

in Fig.5. Fig.6 shows the calculated standard deviation of (a)  $Z_{dr}$ , (b)  $\phi_{dp}$ , and (c)  $\rho_{hv}(0)$  using the alternate method vs  $M$ . The three curves in each panel correspond to the three Doppler spectra shown in Fig.5 whose shapes can be characterized as, (a) narrow, (b) double-peak and (c) wide. The discrete points in Fig.6 are obtained from simulations. The standard deviation of  $\hat{\rho}_{hv}^s(0)$  shown in Fig.6c is very sensitive to spectral shape, while it is not true for  $Z_{dr}$  and  $\phi_{dp}$  as seen in Fig.6a,b.

Fig.7a shows a comparison of the standard deviation of  $\hat{\rho}_{hv}(0)$  using the three estimators  $\hat{\rho}_{hv}^s(0)$ ,  $\hat{\rho}_{hv}^p(0)$  and  $\hat{\rho}_{hv}^F(0)$  for the narrow spectrum shape (Fig.5a). Similar curves are shown in Fig.7b for the double-peak spectrum (Fig.5b), in Fig.7c for the wide spectrum (Fig.5c). Corresponding results for estimates of the mean as a function of  $M$  are given in Fig.8. For the narrow and double-peak spectra shapes, the three estimators are comparable; for good accuracy the power based estimator  $\hat{\rho}_{hv}^p(0)$  is not preferred. For the wide spectrum case (Fig.7c) the alternate and power based estimators give very high standard deviations whereas the FFT based estimator is an order of magnitude better. The mean estimates using the three estimators are comparable for the narrow (Fig.8a) and double-peak (Fig.8b) spectral shapes. For the wide spectrum (Fig.8c) only the FFT method gives a convergent result while the alternate method converges to values slightly greater than unity. Simulation results agree well with radar measurements.

### 4. CONCLUSIONS

We have re-derived the standard derivation and bias of  $\hat{\rho}_{hv}(0)$  for the alternate estimator using the perturbation approach of Balakrishnan & Zrnic (1990). The simulation procedure of Chandrasekar et al. (1986) was used to compare with the perturbation approach and met good agreement. Our results also agree well with the experimental results of Illingworth & Caylor (1991), and Caylor (personal communication). A number of other estimators of  $\rho_{hv}(0)$  were analyzed using simulations. The accuracy in  $\hat{\rho}_{hv}(0) (\pm 0.001)$  for improving polarization estimates of rainfall is likely to be achieved only by simultaneous sampling. For hail detection the accuracy needed is an order of magnitude lower ( $\pm 0.01$ ) which can be achieved using the alternate method if the spectrum is Gaussian, otherwise the FFT based method should be used. Good agreement was found between simulations and the CSU-CHILL radar measurements in convective precipitation.

#### Acknowledgement

This research was supported by the National Science Foundation via ATM-9014600 and AFOSR via grant 91-0141. The CSU-CHILL radar is sponsored by NSF via grant ATM-8919080.

#### References

- Balakrishnan et al., 1990: *J. Atmos. Sci.*, 47(13)
- Chandrasekar et al., 1986: *23rd Conf. Radar Meteor.*
- Doviak et al., 1984: *Doppler Radar and Weather Observ.*
- Illingworth et al., 1991: *25th Conf. Radar Meteor.*
- Oppenheim, A.V. et al., 1983: *Signals and Systems*
- Sachidananda et al., 1989: *J. Atmos. Oceanic Tech.*, (6)

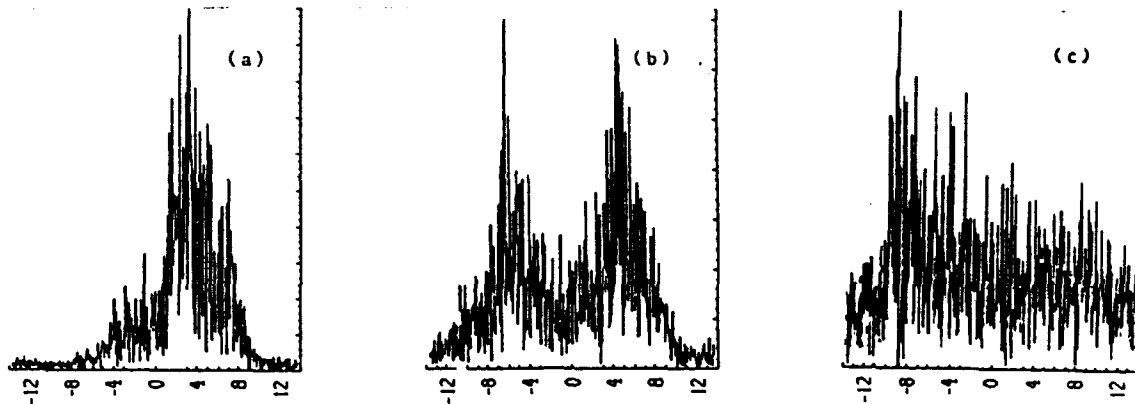


Fig.5 Spectrum of radar data: (a) narrow; (b) double peak; (c) wide.

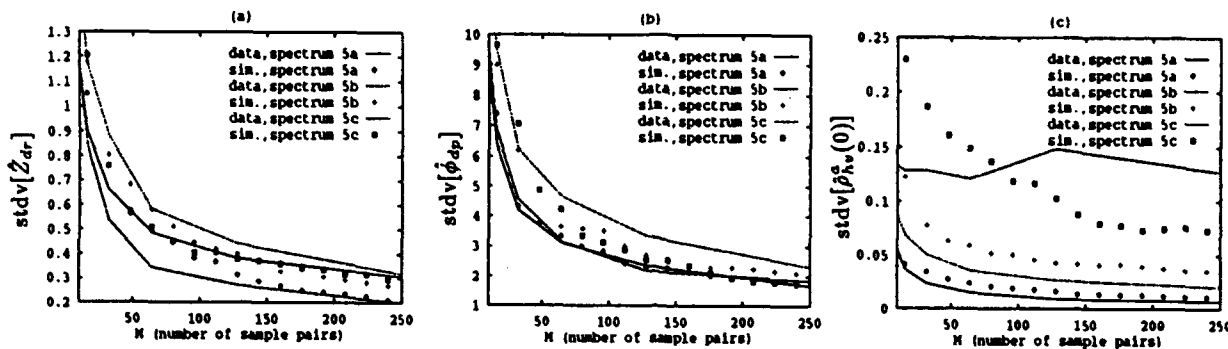


Fig.6 (a)  $\text{stdv}[Z_{dr}]$ , (b)  $\text{stdv}[\phi_{dp}]$ , (c)  $\text{stdv}[\rho_{hv}^a(0)]$  from data and simulation with spectrum of Fig. 5 a,b,c, respectively.

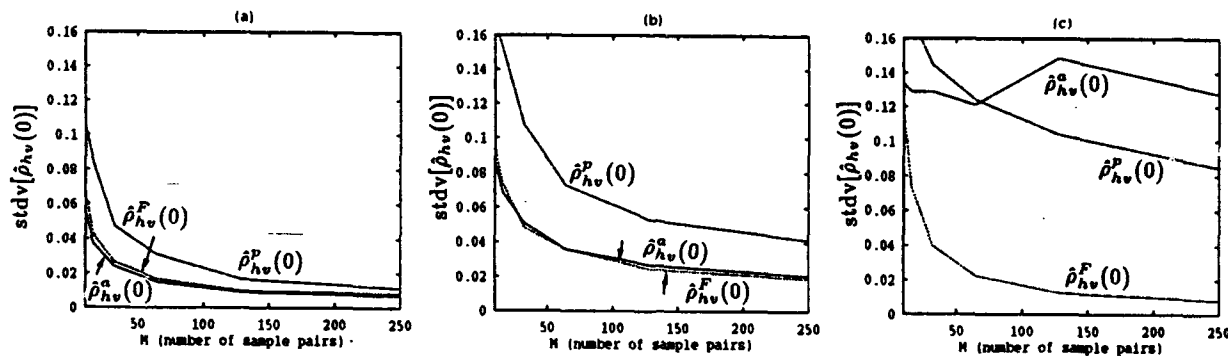


Fig.7 (a)  $\text{stdv}[\rho_{hv}^a(0)]$ , (b)  $\text{stdv}[\rho_{hv}^p(0)]$ , (c)  $\text{stdv}[\rho_{hv}^f(0)]$  from data with spectrum of Fig. 5 a,b,c, respectively.

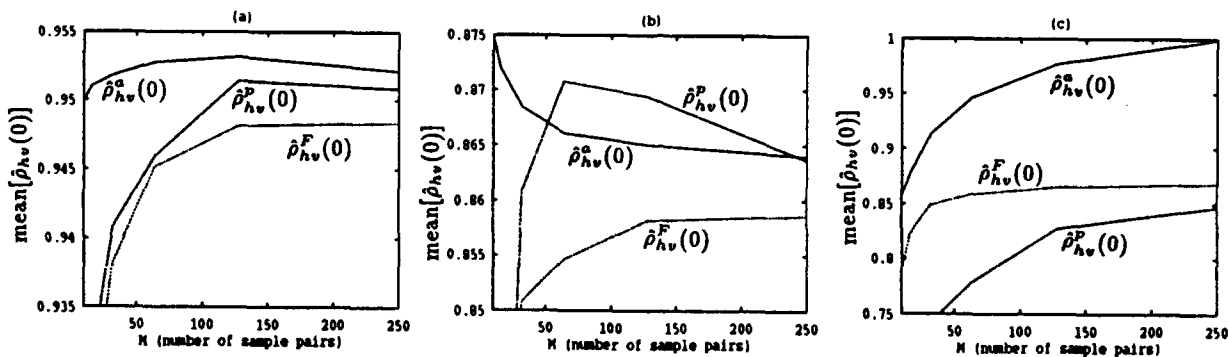


Fig.8 (a)  $\text{mean}[\rho_{hv}^a(0)]$ , (b)  $\text{mean}[\rho_{hv}^p(0)]$ , (c)  $\text{mean}[\rho_{hv}^f(0)]$  from data with spectrum of Fig. 5 a,b,c, respectively.

# Lightning Echoes and Signatures of Pre-lightning Clouds Using a Multiparameter Radar

I.J. Caylor, V. Chandrasekar and V.N. Bringi

Colorado State University

Fort Collins, CO 80523

Tel: 303-491-5420

Fax: 303-491-2249

email: jcaylor@longs.lance.colostate.edu

## Abstract

Observations of lightning echoes by the NCAR CP-2 multiparameter radar in central Florida during the 1991 CaPE project are presented. These observations are unique in that they are at dual wavelength and dual linear polarization and add new polarimetric information to the radar characterization of the lightning echo. An auxiliary signal processor was used during CaPE to make the first polarimetric S-band measurements of the differential phase shift and copolar correlation factor of the lightning echo. The echoes were observed above the melting level with a fixed beam at ranges of 35 to 130 km and at various heights between 5 and 12 km. Using time integrated radar data, statistics for the lightning echo are presented for the S- and X-band reflectivities ( $Z_{10}$ ,  $Z_3$ ), differential reflectivity ( $Z_{DR}$ ), linear depolarization ratio (LDR), differential phase shift ( $\phi_{DP}$ ) and the zero lag copolar cross-correlation ( $|\rho_{HV}(0)|$ ). The statistics confirm that lightning is more readily detected at S-band than X-band and indicate that  $|\rho_{HV}(0)|$  coupled with  $Z_{10}$  is a strong signature for lightning as shown in Figure 1. In addition, there is a strong backscatter differential phase shift of up to  $15^\circ$  associated with the lightning echo. A program was carried out during CaPE to artificially trigger lightning using wire trailing rockets. CP-2 observations are presented in which polarimetric signatures are identified that distinguish between clouds where lightning was successfully triggered and those in which triggering failed. In general the LDR bright band signature clearly indicates triggering is less successful in clouds composed of low density ice crystals aloft and more successful in clouds where LDR indicates higher concentrations of graupel. In addition, the results from an analysis of radar time-series of a rocket triggered lightning observed near ground level are compared to the statistics from natural lightning echoes in the upper levels of thunderstorms.

Presentation format preference: Poster

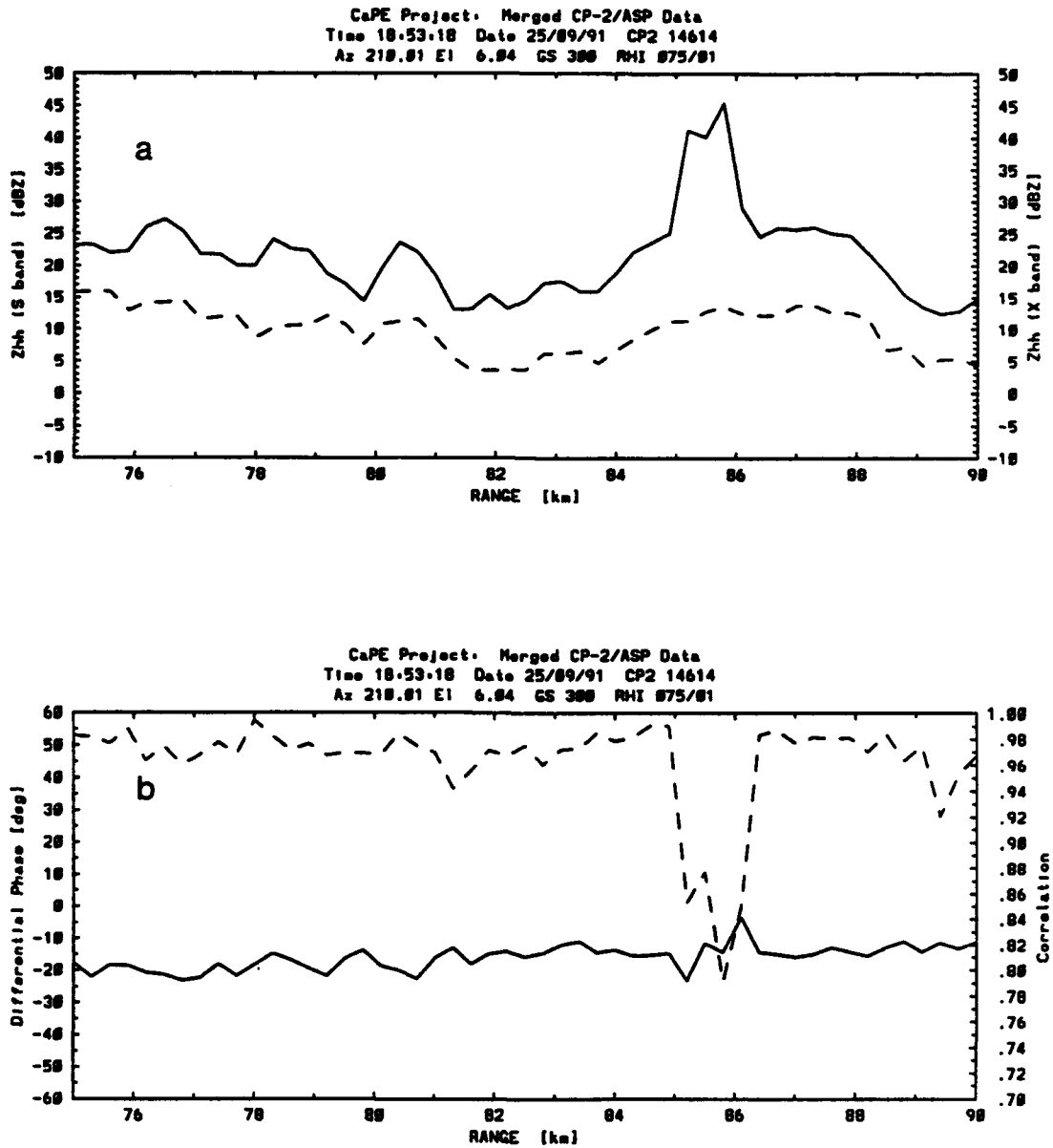


Figure 1. A range profile of a lightning echo: a) showing enhanced echo in S-band reflectivity (solid) at 85-86 km but no increase in X-band (dashed). Note that X-band power has been attenuated due to heavy precipitation at closer range (not shown). b) showing approximately  $\pm 10^\circ$  backscatter phase shift on the  $\phi_{DP}$  profile (solid) and the very large decrease in  $|\rho_{HV}(0)|$  (dashed) at 85-86 km range.

## OBSERVATIONS OF ELECTRIFICATION IN CaPE THUNDERSTORMS

Andrew G. Detwiler, John H. Helsdon, Dennis J. Musil,  
Rahul Ramachandran, and Paul L. Smith

Institute of Atmospheric Sciences  
South Dakota School of Mines and Technology  
Rapid City, South Dakota 57701-3995

and

V. N. Bringi and I. J. Caylor

Department of Electrical Engineering  
Colorado State University  
Fort Collins, Colorado 80523

### 1. INTRODUCTION

The Convection and Precipitation/Electrification (CaPE) experiment was conducted in east central Florida during the period 8 July through 18 August 1991. One of the themes of CaPE was coordinated studies of the co-evolution of the kinematic, microphysical, and electrical properties of Florida thunderstorms. We were fortunate to successfully perform such coordinated studies on several occasions, using instrumented aircraft, radar, and surface instrumentation networks. We discuss here observations of three storms to illustrate the development of precipitation and electrification in loosely-organized multicellular Florida thunderstorms.

### 2. 29 JULY 1991 CASE

The South Dakota School of Mines and Technology (SDSMT) T-28 was launched on this day in anticipation of a boundary outflow collision to the southwest of the multi-parameter CP-2 radar. The storms developed as forecast along the collision zone. The T-28 made multiple penetrations of one cell (cell A,  $X = -17.6$  km,  $Y = -18.6$  km from the CP-2) at 2137 UTC and another cell (cell B,  $X = -21.8$  km,  $Y = -12.15$  km from the CP-2) at approximately 2154 UTC. Here we follow the evolution of cell A.

---

*Corresponding author:* A. G. Detwiler,  
Institute of Atmospheric Sciences, S.D. School  
of Mines and Technology, 501 E. St. Joseph  
Street, Rapid City, SD 57701-3995.

Cell A was first detected by the radar at 2128 UTC. By 2130, its maximum echo intensity had increased to 25 dBz. The echo top at this time was at 6 km MSL ( $-9^{\circ}\text{C}$ ). The CP-2 radar at this time showed a "positive ZDR column" (indicating a region of liquid raindrops) extending up to 4 km ( $4^{\circ}\text{C}$ ).

Figure 1a depicts the time-height cross-section of the cloud evolution from 2130 for a period of 1200 seconds (20 minutes). The 2-dB ZDR maximum height contour (indicating qualitatively the maximum altitude at which large liquid raindrops can be found in the cloud) decreased from 4 km ( $+4^{\circ}\text{C}$ ) gradually for 750 seconds, after which moderately strong updraft (as measured by the T-28) carried it back up to 4.5 km (near  $0^{\circ}\text{C}$ ). Following this, the height fell rapidly, indicating fallout of the raindrops. Figure 1b combines the reflectivity and LDR history of the cell. Regions of high LDR values are observed after 800 seconds at around 3 km ( $+10^{\circ}\text{C}$ ) lying well within the high reflectivity core, perhaps indicating a region of mixed precipitation; i.e., raindrops with wet graupel.

The upper panels in Fig. 1 depict the periods of T-28 penetrations and the range of vertical electrical fields observed during these periods. The T-28 made its first penetration through this cell at 2137 UTC (420 s in Fig. 1) at an altitude of 5.5 km ( $-6^{\circ}\text{C}$ ). By this time, the peak reflectivity had increased to 50 dBz, as also seen in Fig. 2, and the top of the positive ZDR column had fallen below 4 km ( $+4^{\circ}\text{C}$ ). During this first penetration, the T-28 encountered weak updrafts and downdrafts along with graupel and very small amounts of cloud water. The electric field was weak and

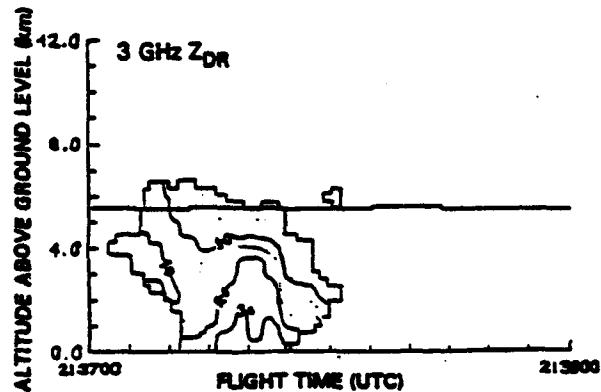
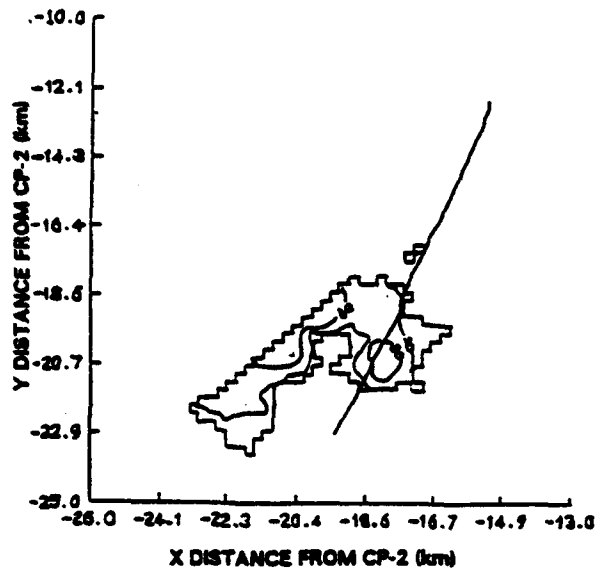


**Figure 2:** (a) CAPPI at  $Z = 5.5$  km at 2137. (b) Vertical cross-section depicting the  $Z_{DR}$  contours at 2137 along the path of T-28 flight.

mainly negative, indicating positive charge above or negative charge below 5.5 km.

The storm subsequently rejuvenated. By 2143 UTC (780 s in Fig. 1), it had grown considerably in size; the second T-28 penetration began at this time. Figure 3 depicts a CAPPI section of the cell at aircraft altitude and the ZDR column along with a vertical cross-section of ZDR along the aircraft track. The top of the 2-dB ZDR column had climbed to 4.5 km ( $0^{\circ}\text{C}$ ) and the echo top to around 9 km ( $-25^{\circ}\text{C}$ ). A vertical radar reflectivity cross-section along the track of the T-28 shows peak reflectivity of 55 dBz at about 4 km ( $+4^{\circ}\text{C}$ ) and a rain shaft falling to near the ground. The maximum updraft and downdraft speeds encountered by the T-28 during

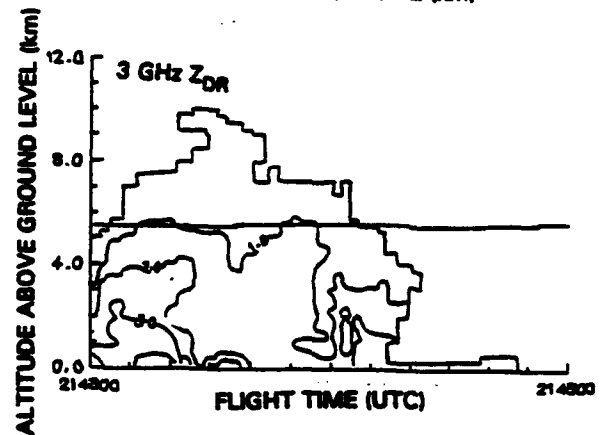
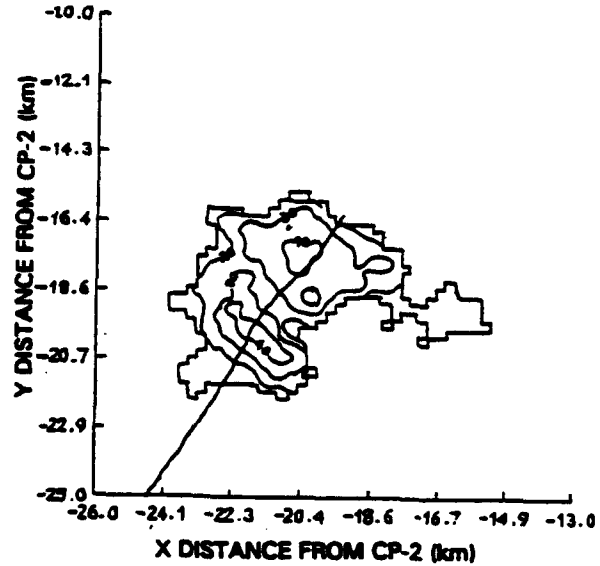


**Figure 3:** (a) CAPPI at  $Z = 5.5$  km at 2143. (b) Vertical cross-section depicting the  $Z_{DR}$  contours at 2143 along the path of T-28 flight.

this penetration at 5.5 km ( $-6^{\circ}\text{C}$ ) were around 5 m/s and the predominant hydrometeor type encountered was graupel. The aircraft's electric field mills recorded positive vertical electric field for this penetration with a maximum value of  $-13$  kV/m, consistent with negative charge above and/or positive charge below the flight level.

A CP-2 scan at 2146 (960 s in Fig. 1), right after the aircraft had exited the cloud, shows precipitation falling to the ground (i.e., the maximum echo intensity had reached close to the ground). At this time, the top of the 2-dB ZDR column had fallen well below the  $0^{\circ}\text{C}$  level, indicating fallout of the main precipitation core associated with a weakened updraft.

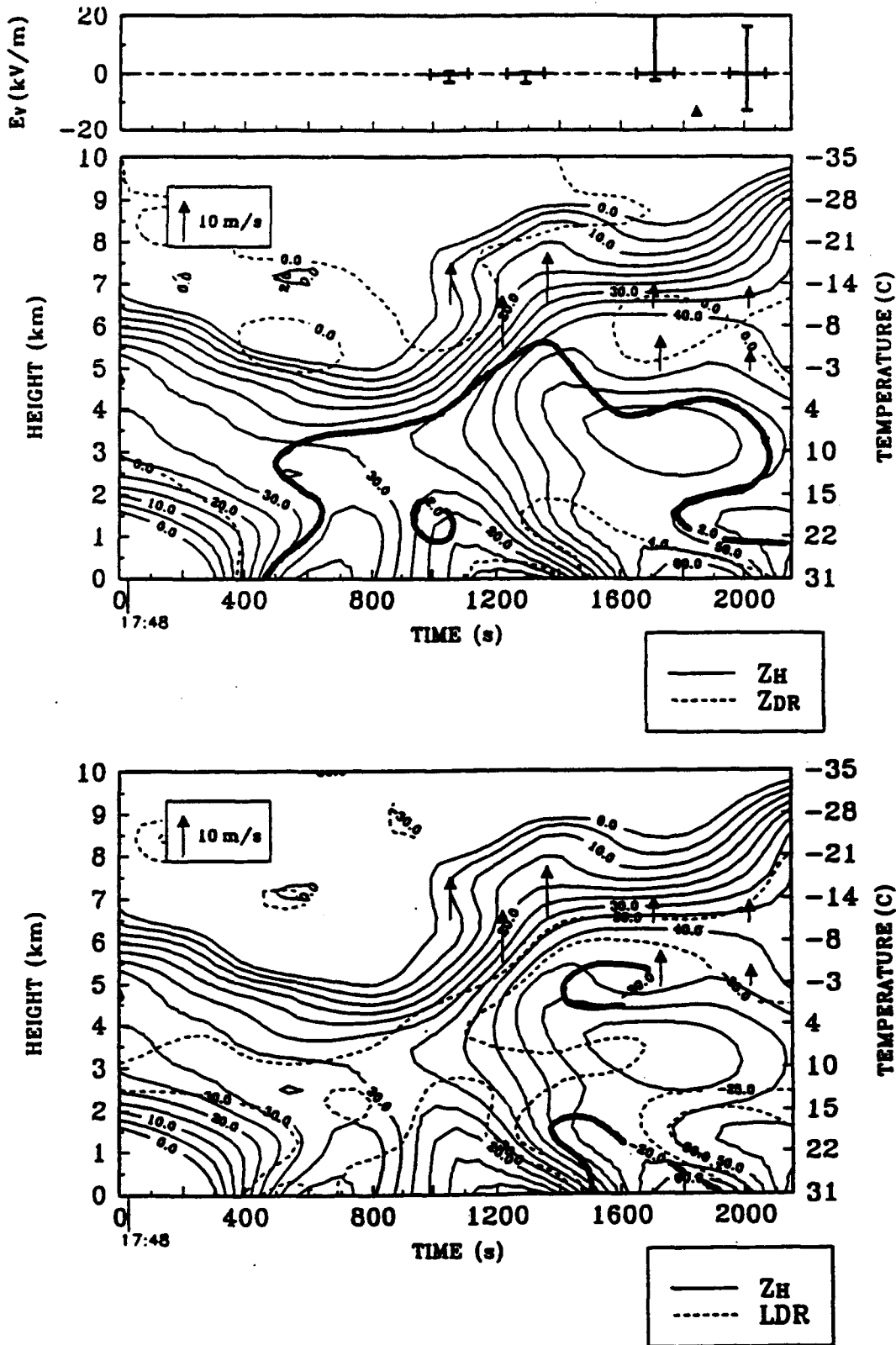


Figure 4: Same as Fig. 1, but for cell detected at 1748 on 9 August. 2 dB ZDR and -20 dB LDR contours have been highlighted.

Organized updrafts and downdrafts were found by aircraft penetrating in the 5 to 6 km altitude range (-5 to -9°C) at the time electrification was first detected, but downdrafts were not usually present before this. Measurable vertical electric fields first detected at these levels were associated with the downdraft regions containing graupel rather than with the updraft regions containing cloud water with low concentrations of rain.

Takahashi (1978) found that, at temperatures above -10°C, ice spheres became positively charged during collisions with smaller ice crystals. However, at lower temperatures the charging was a function of cloud liquid water concentration. At either high or low liquid water concentrations, ice spheres acquired positive charge; they acquired negative charges when moderate cloud water concentrations were present. Gaskell and Illingworth (1980) found similar results, indicating that precipitation-size ice particles got positively charged during collisions with small ice crystals at temperatures in the range -5 to -10°C and negatively charged at -15 to -20°C.

Most aircraft penetrations in the three storms discussed here were in the -4 to -10°C temperature range. The predominant sign of the vertical electric field was positive, consistent with positive charge below and/or negative charge above the aircraft. Thus the *in situ* vertical electric field measurements are consistent with laboratory results for non-inductive ice particle collision charging mechanisms. Particularly, on the last penetration of the storm on 29 July, when the aircraft was near the radar top of the storm at 5.5 km (-6°C), it is almost certain that if the precipitation particles at and below this level were carrying charge, this charge was positive.

As these clouds develop microphysically, they also are evolving dynamically. Initially the visible cloud is almost completely updraft with compensating downdrafts in the clear air outside the cloud, so weak as to be almost undetectable by aircraft. As rain forms by coalescence of cloud droplets within this updraft, it is carried upward. It may freeze just above the freezing level (typically when the convection is weak and/or disorganized), or perhaps due to ice ingested from a neighboring cloud, or it may remain supercooled to colder temperatures (typical in the case of stronger and more organized convection). As the rain freezes, organized downdrafts develop within

the cloud, carrying the graupel grown upon the frozen-drop embryos from the 5 to 6 km levels to lower levels. The updraft also may start to collapse at this time. Another possibility is that coalescence freezing of raindrops could result in release of latent heat which could invigorate the updraft. In the cases described here, radar cloud top was typically above 8 km (-25°C) at the time the 2-dB ZDR column began to fall back from the 5 km (-4°C) level and electrification began to develop.

## 5. SUMMARY

All three cases tend to show similar signatures. Following vertical development of a positive ZDR column which rises above the freezing level, the raindrops responsible for the positive ZDR freeze and form a region of high LDR values aloft. This is followed by a subsequent increase in the vertical electric field values associated with downdraft regions in the cloud containing wet graupel. Mixed-phase microphysics plus updraft/downdraft structures therefore appear to play an important role in electrification of a cloud.

A plausible explanation for the lack of cloud-to-ground lightning for the 29 July case could be that the cloud was not very convective nor long-lived. Its updrafts were weak (maximum measured updrafts were -5 m/s) and short-lived. The storms on 9 August were more organized and grew to greater depths, allowing more complete development of precipitation and electrification processes.

*Acknowledgments.* This research was sponsored by the National Science Foundation under Grant Nos. ATM-9014600, ATM-9022846 and Cooperative Agreement No. ATM-9104474, the Air Force Office of Scientific Research under Grant No. 91-0141, and by the NOAA/North Dakota Cooperative Agreement No. NA 27RA0178-01 under Contract No. ARB-IAS-92-1 through the North Dakota Atmospheric Resource Board.

## REFERENCES

Bringi, V. N., I. J. Caylor, J. Turk and L. Liu, 1993a: Microphysical and electrical evolution of a convective storm using multiparameter radar and aircraft data during CaPE. Preprints, 26th Intl. Conf. on Radar Meteor., Norman, OK, Amer. Meteor. Soc., 312-317.

# MULTIPARAMETER RADAR OBSERVATIONS OF LIGHTNING

I.J. Caylor, V. Chandrasekar, V.N. Bringi and S.S. Minger

Colorado State University  
Fort Collins, CO 80523

## 1. INTRODUCTION

Observations of lightning were made in central Florida during the 1991 Convective and Precipitation/Electrification experiment (CaPE) with the NCAR CP-2 multiparameter radar. Williams et al. (1989) have reported single polarization radar observations of lightning at UHF, S-band, and C-band while more recently Krehbiel et al. (1991) have employed a wideband polarimetric radar at X-band. The CaPE observations presented in this paper are unique in that they were made simultaneously at S- and X-band wavelengths with dual linear polarization.

One of the questions concerning the radar observation of lightning deals with the temperature of the plasma channel. Most recently Holmes et al. (1980) have interpreted their data in terms of a low temperature (underdense) while Williams et al. (1989) have supported the theory of a hot (overdense) plasma. An overdense plasma is a highly conducting target at conventional radar wavelengths and difficulty in detecting lightning at short wavelengths is explained by masking of the lightning by the precipitation echo. The data presented below address this question and the additional polarimetric information provides insight into the spatial geometry of the lightning echo.

## 2. OBSERVATIONS

The CP-2 radar operates with a PRF of 960 Hz at a dual wavelength of 3.2 and 10.7 centimeters. The S-band system is coherent and provides estimates of reflectivity ( $Z_s$ ) and differential reflectivity ( $Z_{DR}$ ). During CaPE an auxiliary signal processor was implemented on the S-band receiver providing real-time measurements of the differential phase shift ( $\phi_{DP}$ ) between the horizontal and vertical returns and, the correlation coefficient ( $|\rho_{HV}(0)|$ ) between H and V returns (Chandrasekar et al., 1993). The X-band system provides estimates of the reflectivity ( $Z_x$ ) and linear depolarization ratio (LDR).

The data described in this paper were collected with the CP-2 radar in a manual mode with the beam stationary in both azimuth and elevation. The X- and S-band antennas have coaxial beams with a width of about  $1^\circ$ .

## 2.1 Natural lightning

The radar signal processor was configured to integrate data for an interval of 128 pulses (64 horizontal and 64 vertical). The typical range gate spacing was 300 m.

Lightning echoes were observed in thunderstorms above the freezing level at heights between 5 and 12 km and at slant ranges between 35 and 130 km. Figure 1 shows a range profile with a typical lightning echo between 55.5 and 59 km. The lightning is particularly visible as a marked drop in  $|\rho_{HV}(0)|$  and an increase of  $Z_s$  with a peak excursion of 25 dB above the precipitation echo (58 km). Note the small enhancement of  $Z_x$ .

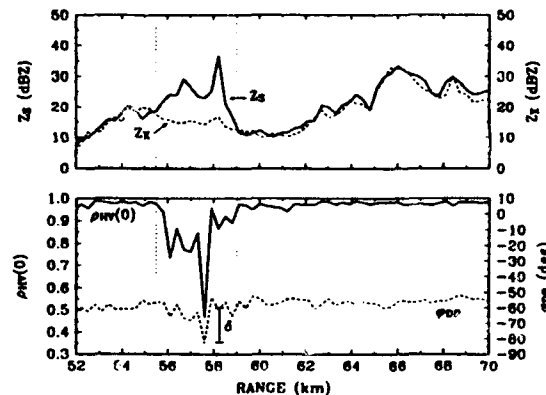


Figure 1. Range profile showing a lightning echo at 55.5 to 59 km. The elevation is  $5.58^\circ$  corresponding to height 5.5 km above ground level.

Range profiles as in Figure 1 were processed to isolate the lightning echo. The profiles were thresholded on an S-band SNR of 30 dB removing weak, noisy signals. The lightning signature was then isolated by flagging points in the profile where  $Z_s$  deviated by 2.0 dB and  $|\rho_{HV}(0)|$  deviated by 0.075 from their respective means. The mean for each parameter was computed by averaging 10-15 profiles ( $\sim 1.5$  s) prior to the lightning. The flagged lightning echoes were extracted for further analysis.

24 events spread over 6 different days were selected for this paper from the events logged during the CaPE

campaign. It is worth noting that typically the duration for each event spanned two or more integration cycles and extended over several kilometers range. Therefore 155 data points were available for statistic analysis.

Using data extracted from the lightning signatures, the distribution of  $\eta$  (reflectivity in units of cross-section per unit volume) is shown in Figure 2 for X- and S-band. The corresponding distributions  $Z_{DR}$ , LDR, and  $|\rho_{HV}(0)|$  are shown in Figures 3, 4, and 5.

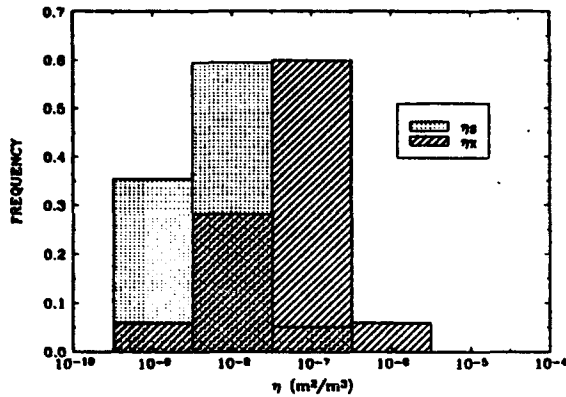


Figure 2. Reflectivity distributions for S-band and X-band. The mean for  $\eta_s$  is  $3 \times 10^{-8} \text{ m}^2/\text{m}^3$ , while the mean for  $\eta_x$  is  $3 \times 10^{-7} \text{ m}^2/\text{m}^3$ .

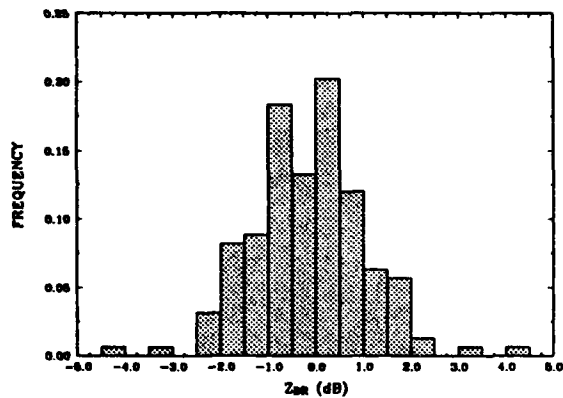


Figure 3. The differential reflectivity distribution with a mean value of -0.2 dB and  $\sigma = 1.2$  dB.

The differential phase shift upon backscatter ( $\delta$ ) was estimated by subtracting  $\phi_{DP}$  for each lightning echo from the computed mean  $\phi_{DP}$  profile. A histogram of the estimated  $\delta$  is shown in Figure 6.

## 2.2 Triggered lightning

During the CaPE campaign, NASA and French teams engaged in triggered lightning experiments using wire

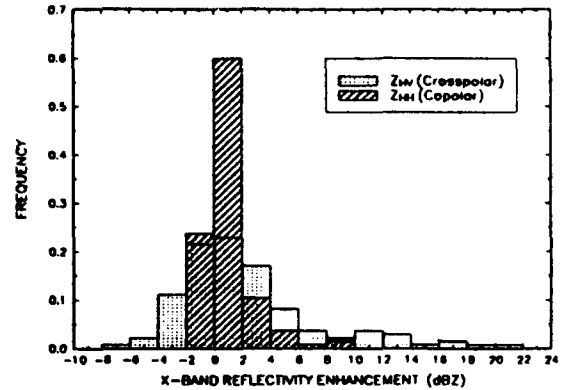


Figure 4. Distributions of the enhancement of the copolar and cross-polar X-band reflectivities due to lightning.

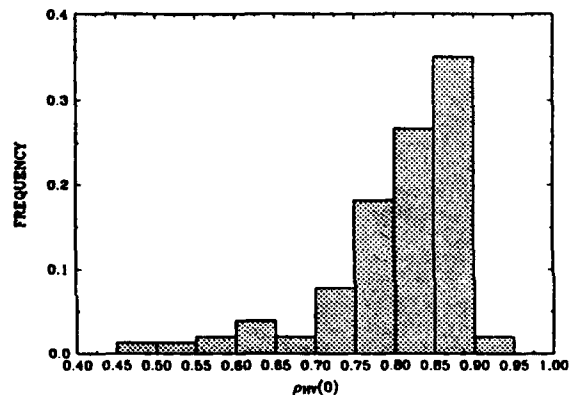


Figure 5. Distribution of the copolar correlation with a mean of 0.8 and  $\sigma = 0.086$ .

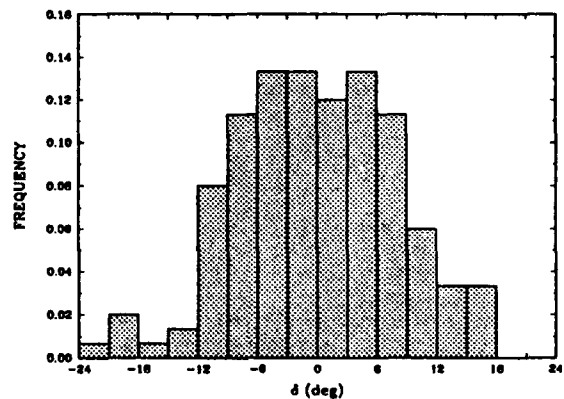


Figure 6. Distribution of backscatter differential phase shift with a mean of  $0.7^\circ$  and  $\sigma = 9.5^\circ$ .

trailing rockets. The land-based launch site was located approximately 7 km to the south east of CP-2. On 25 August 1991, lightning was triggered at 17:50:57.130 GMT at which time the CP-2 antenna was positioned over the launch site at an elevation of 5° (height = 610 m). The RP-6 signal processor was in a time-series collection mode with a range gate spacing of 250 m and an integration interval of 256 pulses.

There was very little precipitation over the launch site at the time of the triggering and so precipitation masking is negligible. The radar echo had a duration of approximately 500 ms, a  $Z_{DR}$  of -4 dB,  $Z_s$  of 32 dBZ.

### 3. DISCUSSION

If a power law dependence on wavelength is assumed for lightning reflectivity ( $\eta \propto \lambda^n$ ), the value of  $n$  can be computed from simultaneous observations at two wavelengths. For each S- and X-band data pair (Fig. 2) the exponent was computed. The results in Figure 7 show a mean value near -2 and support the  $\lambda^{-2}$  dependence found by Williams et al. (1989) who used UHF, S- and X-band.

The time series for the triggered lightning were analyzed in a similar manner with the exponent being computed for each pair of dual wavelength pulses. Surprisingly the mean value for  $n$  is near +1.5 (Fig. 7). A straightforward interpretation of this result is that the channel is underdense. However video photography of the triggered lightning indicates the channel had a large 3 dimensional curvature and so it is possible that the lightning was being observed in the antenna sidelobes. Further analysis of these time series, including a Doppler spectral analysis, along with ground based electrical data is planned.

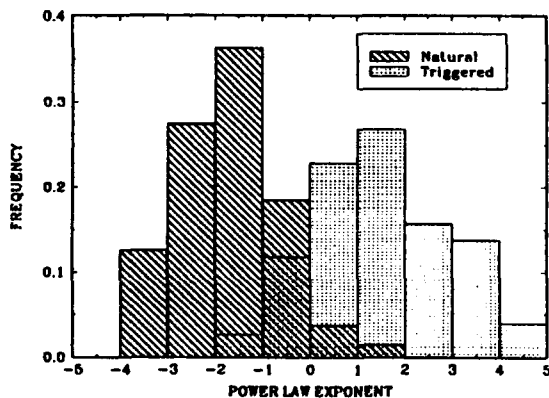


Figure 7. Distribution of the power law exponent,  $n$ , for natural (mean of -1.7) and triggered lightning (mean of 1.5).

In general the polarimetric signatures (Figs. 3-6) indicate the lightning target is geometrically complex. The wide variation of  $Z_{DR}$  and  $\delta$  with means near zero indicate no preferred orientation of the target. The 2.4 dBZ enhancement of the X-band crosspolar reflectivity is indicative of a randomly oriented target as well.

Analysis shows that decreases in  $|\rho_{HV}(0)|$  are not correlated with large  $\delta$ . This could be due to multiple scattering interactions between individual lightning elements within the pulse volume.

### 4. CONCLUSION

Multiparameter radar observations of natural lightning during the CaPE project show the following:

- The parameter  $|\rho_{HV}(0)|$  decreases dramatically for the lightning echo and coupled with  $Z_s$  is an excellent polarimetric signature for lightning.
- There is a  $\lambda^{-2}$  dependence between X-band and S-band reflectivities for lightning in precipitation.
- X-band cross-polar results indicate the lightning echo is depolarizing.  $Z_{DR}$  data show that there is no apparent channel orientation. In addition there is a large backscatter differential phase shift of up to  $\pm 15^\circ$  which is uncorrelated with low  $|\rho_{HV}(0)|$ .
- The only triggered lightning observed during CaPE displays an unusual signature. Further observations of triggered lightning would be of great benefit.

*Acknowledgements.* The authors thank Dr. Paul Krehbiel for his assistance in making the lightning observations during CaPE. Funding for this work was provided by the National Science Foundation (ATM-9014600) and U.S. Air Force (AFOSR 91-0141).

### 5. REFERENCES

- Chandrasekar, V., G.R. Gray, and I.J. Caylor, 1993: Auxiliary signal processing system for a multiparameter radar. *J. Atmos. Oceanic Technol.*, in press.
- Holmes, C.R., E.W. Szymanski, S.J. Szymanski, and C.B. Moore, 1980: Radar and acoustic study of lightning. *J. Geophys. Res.*, **85**, 7517-7532.
- Krehbiel, P.R., W. Rison, S. McCrary, T. Blackman, and M. Brook, 1991: Dual-polarization radar observations of lightning echoes and precipitation alignment at 3 cm wavelength. *Proc. 25th Conf. Radar Meteorology*, Paris, Amer. Meteor. Soc., 901-904.
- Williams, E.R., S.G. Geotis, and A.B. Bhattacharya, 1989: A radar study of the plasma and geometry of lightning. *J. Atmos. Sci.*, **46**, 1173-1185.

# MULTIPARAMETER RADAR AND AIRCRAFT STUDY OF THE TRANSITION FROM EARLY TO MATURE STORM DURING CaPE: THE CASE OF 9 AUGUST 1991

V.N. Bringi, A. Detwiler\*, V. Chandrasekar, P.L. Smith\*, L. Liu, I.J. Caylor and D. Musil\*

Colorado State University, Fort Collins, CO

\* South Dakota School of Mines and Technology, Rapid City, SD

## 1. INTRODUCTION

On 9 August, 1991, convection began forming over the Cape Canaveral area at 16:30 UTC due to interactions between horizontal convective rolls and river breezes. Surface winds were from the W/NW near the Cape area. The 15:00 sounding at Cape Canaveral indicated light westerly winds up to 6 km which then shifted to E/SE winds above 7.5 km. The 0°C level was at 4.6 km, and cloud base was at 1.2 km. A cloud which developed over the NASA field mill network was subsequently penetrated by the T-28 at an altitude of 4.8 km msl. The CP-2 radar captured the full cloud evolution from first echo through the mature stage. The cloud was first detected (8.5 dBZ at 4.3 km height, range=23.5 km) at 18:21 UTC (henceforth all times are UTC and all heights are msl). For a few minutes the dual-frequency (S/X-band) reflectivity ratio, DFR, was 8 - 9 dB giving evidence of partial Bragg scattering, the  $Z_{dr}$  being 0 dB. At 18:25,  $Z_h$  increased to 10 dBZ, the DFR decreased to 0 dB while  $Z_{dr}$  jumped to 1.7 dB at 5 km height. This, we believe, is strong evidence for raindrop formation by the warm rain process. At 18:28 a few big drops ( $Z_{dr} \sim 3 - 4$  dB) were detected falling to the ground while an anvil from a mature storm (about 10 km to the SE) extended over the cloud of interest at 9 km height. It appears from the radar data that ice crystals from the anvil descended into the upper part of this cloud, freezing it.  $Z_{dr}$  was nearly 0 dB above 5.5 km, with large drops continuing to fall out from the cloud. The reflectivity aloft (6 km) intensified to 48 dBZ at 18:36 with  $Z_{dr}$  being 0 dB, indicating graupel formation. We refer to this cloud as cell A, to distinguish it from new growth that occurred on the NW side of cell A, a region with persistent updraft. The first evidence of new growth was at 18:35 and this cloud will be called cell B as its evolution could be separately tracked. Its microphysical evolution was rapid and very different from cell A and was responsible, we believe, for cloud electrification which started at 18:41 with the first CG strike at 18:43.

## 2. CLOUD EVOLUTION

Fig.1 shows CAPPIs at 5.5 km height with T-28 tracks which penetrated the cloud at 18:36 and 18:41 overlaid. The grey scales depict  $Z_{dr}$ , the darker shades representing larger values. Fig.1a shows cell A about 12 min after first echo. Fig.1b shows a positive  $Z_{dr}$  column (cell B) while cell A has glaciated ( $\sim 0$  dB  $Z_{dr}$ ). Fig.2 shows vertical sections taken along the shear direction (SE-NW);

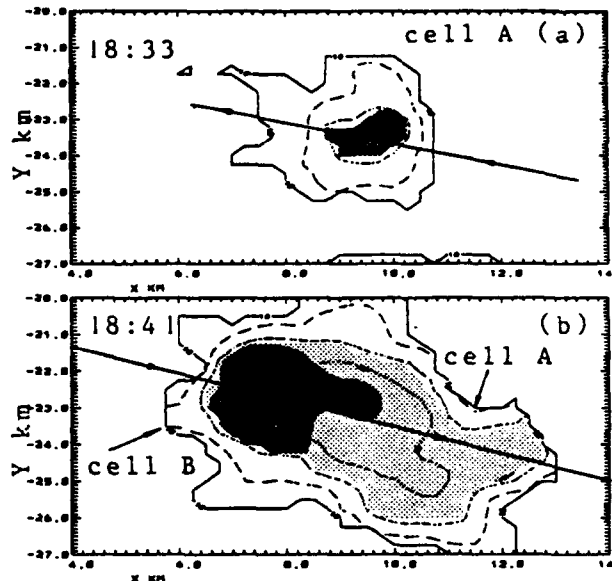


Fig.1 CAPPi at 5.5 km height of  $Z_h$  contours (start from 10 dBZ, step 10 dB) with  $Z_{dr}$  grey scales (the intervals being 0.5,1.5,3,4 dB).

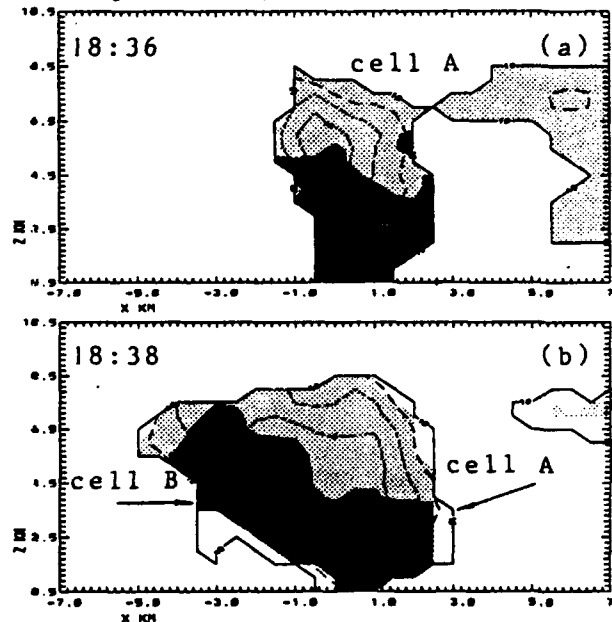


Fig.2 Vertical sections along an SE-NW line in Fig.1. X=0 here is the center of the reflectivity core in Fig.1.  $Z_{dr}$  grey scales same as in Fig.1.

positive (negative) X values represent locations SE (NW) of the main echo. Note the positive  $Z_{dr}$  column in Fig.2b (cell B). The height profile of  $Z_{dr}$  represents updraft conditions in cell B and downdraft in cell A. Fig.3 summarizes T-28 data for the 18:36 (solid lines) and 18:41 (dashed lines) penetrations, which were respectively along the SE — NW and NW — SE directions. At 18:36 the T-28 detected a peak downdraft of 9 m/s just below the main echo in Fig.2a (cell A). The PMS 2D-P probe as well as the Cannon camera showed a mixture of very wet graupel and drops in the downdraft with maximum sizes of 6 - 7 mm as shown in Fig.3. The LDR was about -23 dB in the downdraft, consistent with wet graupel. A peak updraft of 13 m/s (LWC  $\sim 1.5 \text{ g/m}^3$ ) was detected about 2.5 km NW of the main echo in Fig.1a. This was well correlated with the first radar detection of cell B at 18:36 at 5 km height. The T-28 pilot reported moderate rain early during penetration of the updraft. Neither the P-probe nor the Cannon camera detected any drops in the updraft; however, the foil impactor registered a few circular impressions (drops) of 1-2 mm diameter in the updraft. On the return penetration at 18:41, the T-28 sampled cell B (updraft peak  $\sim 15 \text{ m/s}$ , LWC  $\sim 2 \text{ g/m}^3$ ) and cell A (downdraft peak  $\sim 7 \text{ m/s}$ , wet graupel 6 - 7 mm). Within the updraft (positive  $Z_{dr}$  column, Fig.2b), the P-probe detected a few large drops (5 - 6 mm) while the foil impactor registered eight circular impressions, the largest being 2.5 mm, and about 10s later a large drop ( $\sim 6 \text{ mm}$ ). The T-28 pilot reported moderate rain in the updraft. These data are consistent with the positive  $Z_{dr}$  column in Fig.2b (cell B) consisting of a low concentration of large drops. The pilot also reported lightning during this penetration as well as a transition from rain to ice on the windscreen as he left the updraft. A dry/wet growth modeling calculation showed that the larger graupel (6 - 7 mm) could be in wet growth. Peak LDR and X-band specific attenuation values of -18 dB and 1 dB/km were observed at the T-28 flight altitude in the downdraft, which are also consistent with wet graupel.

Fig.4a shows the time-height reflectivity profile of cell A starting at 18:23; contours start at 0 dBZ and increment by 5 dB. The dark solid line shows the maximum height reached by the 2 dB  $Z_{dr}$  contour. Note the overlying anvil from a mature storm about 10 km to the SE referred to earlier. The arrows represent peak vertical winds from the T-28 penetrations at 18:36, 18:41 and 18:48 and one penetration of the NOAA P-3 at 18:45. The top panel shows the vertical electric field from a surface field mill located under the cloud at X=13, Y=-24 km (see Fig.1b). The dark vertical bars are the maximum vertical component of the E-field from the T-28 field mills. Horizontal dark bars represent the duration of the penetration. The solid triangle at 1200s is the time of the first cloud-to-ground lightning detected by the NASA LLP network (18:43:27 at X=13.5, Y=-24.6 km). Before 600s the surface field mill activity is due to a strong storm located 10 km W/SW. Fields with fair weather polarity start at 700s with a reversal evident at 900s. At 1050s (18:41 T-28 penetration in Fig.3) the electric fields build up at the T-28 altitude

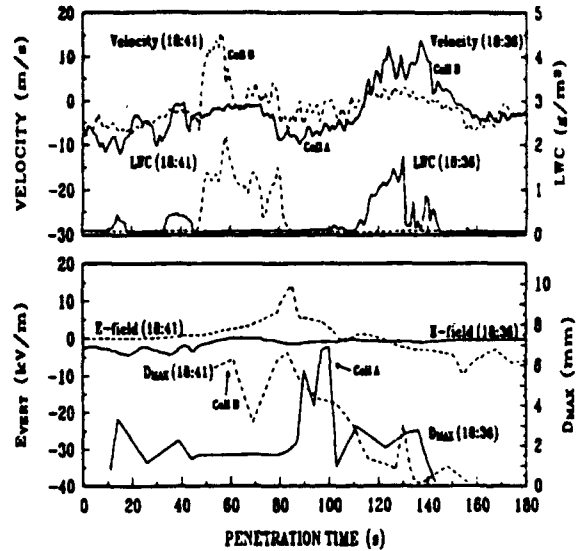


Fig.3 Data from T-28 showing up/downdraft (velocity), liquid water content (LWC), vertical E-field and maximum particle size. The time  $t=0$  is the starting time for each penetration.

with the CG strike following at 1200s. As noted, the T-28 pilot reported lightning during the 18:41 penetration, the surface field mill shows numerous strikes after this time. Cell A shows a general sinking of the reflectivity with time after 700s ( $\sim 18:34$ ) with some indication of pulsation. The maximum height of the 2 dB  $Z_{dr}$  contour also sinks slowly, correlating well with the persistent downdraft measured by the two aircraft.

The evolution of cell B in Fig.4b is quite different. It was first detected as new growth at 700s. The strong updraft detected by the T-28 (Fig.3) correlates well with the positive  $Z_{dr}$  column, the 2 dB  $Z_{dr}$  height rising to 6 km ( $-8^{\circ}\text{C}$ ). Subsequently, following what appears to be freezing of the raindrops the  $Z_{dr}$  height falls while the cloud top grows substantially, possibly due to the associated latent heat release. By the time of the T-28's 18:41 penetration, the 50 dBZ core is at 6.5 km. This was also a region of wet growth as predicted by the growth model. The 2 dB  $Z_{dr}$  height doesn't decrease, remaining near the  $-3^{\circ}\text{C}$  level indicating persistent updraft as corroborated by the P-3 and T-28 penetrations at 18:45 (1350s) and 18:48 (1500s), respectively. The surface field mill located near cell B at X=7, Y=-22 km (see Fig.1) shows fair weather polarity until 1050s ( $\sim 18:40$ ), with subsequent electrification until the CG strikes are indicated (top panel). The T-28 field mills also show electrification at the time. It appears that mixed phase microphysics plus the up/downdraft structure played important roles in electrifying the clouds. Detailed analysis of the aircraft data and other radar signatures such as LDR and  $A_3$  will add important details to the cloud evolution.

#### Acknowledgement

Support for this research came from the National Science Foundation via ATM-9014600, ATM-9022846 and ATM-9104474, and from AFOSR via 91-0141.

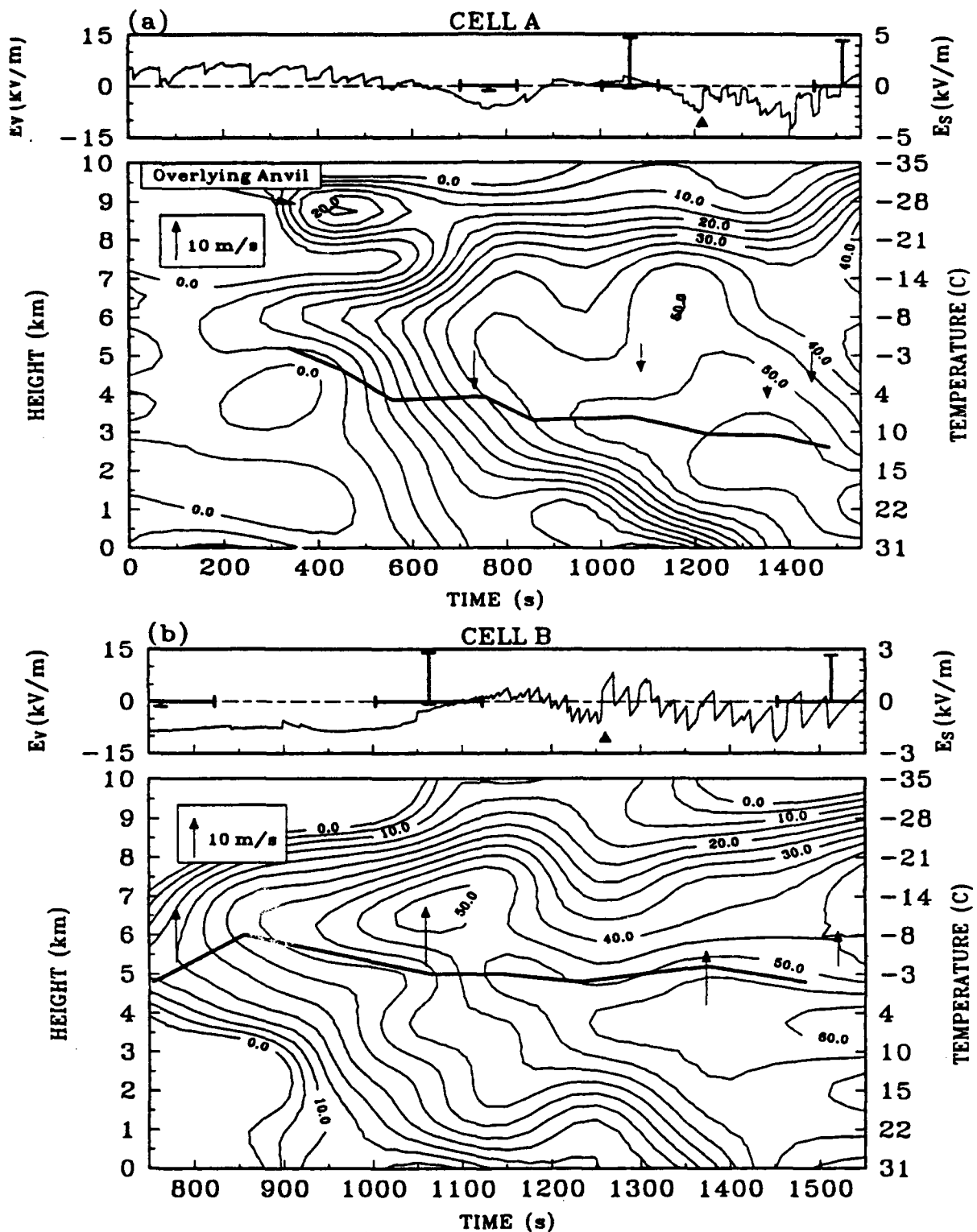


Fig.4 Time-height contours of  $Z_d$  for cell A (a) and cell B (b). Dark solid line is the maximum height of the 2 dB  $Z_d$  level reached at various times. Vertical arrows are peak updraft speeds from T-28 (3) and P-3 (1). Top panels show maximum vertical E-field from T-28,  $E_v$  (dark solid bars), and the E-field from surface field mill located near the cells,  $E_s$  (light continuous line). The solid triangle mark in (a) at 1210 s, and (b) at 1260 s, is the first CG strike from the cell.

INTERCOMPARISON OF MULTIPARAMETER RADAR SIGNATURES FROM FLORIDA STORMS

L. Liu, V.N. Bringi, I. J. Caylor and V. Chandrasekar  
 Colorado State University, Fort Collins, CO 80523

1. INTRODUCTION

The CaPE project offered the first opportunity to collect dual-polarized, dual-frequency radar data in the subtropical regime of central Florida. This paper is based on CP-2 time series data collected at vertical incidence in light rain, and in a squall line case at close range. Each time series record consisted of 128 H and 128 V samples at S-band, and 256 H samples at X-band. From these data, reflectivity at horizontal polarization  $Z_h$ ,  $Z_{dr}$ , copolar correlation coefficient  $\rho_{hv}(0)$ , differential propagation phase  $\phi_{dp}$  and dual-frequency (S/X) reflectivity ratio DFR were calculated. A new algorithm for calculating specific attenuation  $A_3$  at X-band and specific differential phase  $K_{dp}$  is used based on *Hubbert et al. (1993)*, which accounts for hail signal and phase shift upon backscatter fluctuations which may be superimposed on the range profiles of DFR and  $\phi_{dp}$ , respectively.

2. CP-2 RADAR MEASUREMENTS

The radar data reported here were collected on 24 August, 1991 of the CaPE project.

2.1. Vertically Pointing Data

Raindrops at vertical incidence form a standard target for polarization measurements because of rotational symmetry of the drops when viewed vertically. In addition, if the antenna is rotated a full 360°, the polarization plane also rotates with it. For this method to work the melting level must be located beyond the far-field of the antenna (in this case ~ 1.5 km), a common situation in Florida but not in Colorado, for example.

Fig.1 shows vertical profiles of  $Z_h$ ,  $\rho_{hv}(0)$ ,  $\phi_{dp}$ , and DFR in light rain at 90° elevation angle. These data have not been filtered in range. The vertical bars in each case show the sample standard deviation. The  $Z_h$  bright-band is clearly visible at 3.5 km (all heights are agl). The dip in  $\rho_{hv}(0)$  to 0.92 at 3.25 km is also clearly noted. Note that  $\rho_{hv}(0)$  is estimated from the power time series (see *Liu et al., these Proceedings*). The mean value of  $\rho_{hv}(0)$  in light rain below the bright-band is around 0.982. It is well known that  $\rho_{hv}(0)$  should be very close to unity in light rain even at horizontal incidence with values of 0.997 quoted by *Mingworth & Caylor (1991)*. At vertical incidence the deviation from 1 should be even less. One possible reason for the measured  $\rho_{hv}(0)$  being so low is that the phase difference between the HH and VV antenna patterns within the main lobe deviates due to feedhorn imperfections or loss of precision of the reflector shape. Simulations show that this effect is sufficient to drop  $\rho_{hv}(0)$  to 0.99 (see *Xiao et al., these Proceed-*

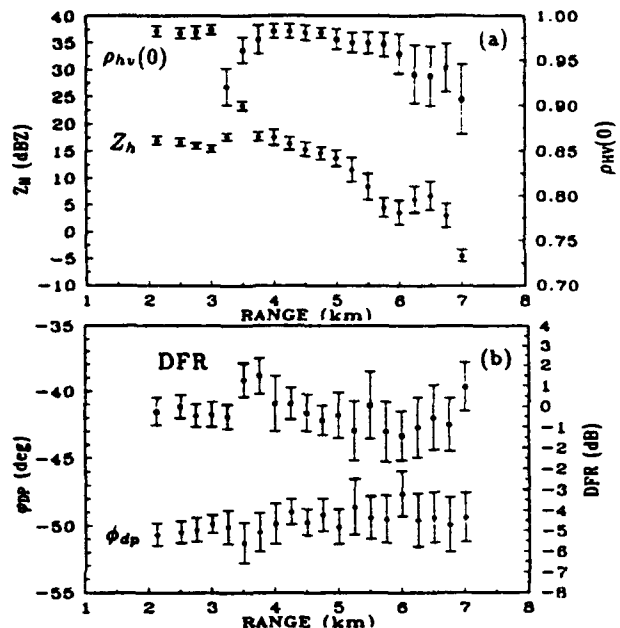


Fig.1 Range profiles of mean and standard deviation of (a)  $Z_h$ , and  $\rho_{hv}(0)$ , (b)  $\phi_{dp}$  and DFR from vertical pointing data.

ings). The increase in  $\sigma$  with height > 5.5 km is due to SNR becoming smaller. The large  $\sigma$  at the  $\rho_{hv}(0)$  dip is consistent with theory (see *Liu et al., these Proceedings*) and with the results of *Mingworth & Caylor (1991)*. The system  $\phi_{dp}$  (~ -50.5°) can be obtained from Fig.1b since at vertical incidence no differential propagation effects are expected in light rain. The DFR results are also shown in Fig.1b. Note the positive fluctuation of about 1.5 dB in the mean at 3.75 km, very close to the peak  $Z_h$ . This is suggestive of Mie scattering effects due to large, wet snowflakes with maximum size around 10 mm. An assessment of the overall accuracy in derived specific attenuation ( $A_3, dBkm^{-1}$ ) and specific differential phase ( $K_{dp}, ^\circ km^{-1}$ ) can be made since the mean should equal zero in light rain. Errors may be due to statistical fluctuations, system effects, and the algorithms used to estimate  $A_3$  and  $K_{dp}$ . Here we use an adaptation of range filters described by *Hubbert et al (1993)* to calculate  $A_3$  and  $K_{dp}$ . The accuracy in estimating the mean value is defined here as the sum of the absolute value of the bias and the 95% confidence interval which is 0.2 - 0.25 ( $dBkm^{-1}$  or  $^\circ km^{-1}$ ) for both  $A_3$  and  $K_{dp}$ . Note the condition at vertical incidence, i.e., high SNR, narrow spectrum width and very high  $\rho_{hv}(0)$ .

2.2. Rainfall Data

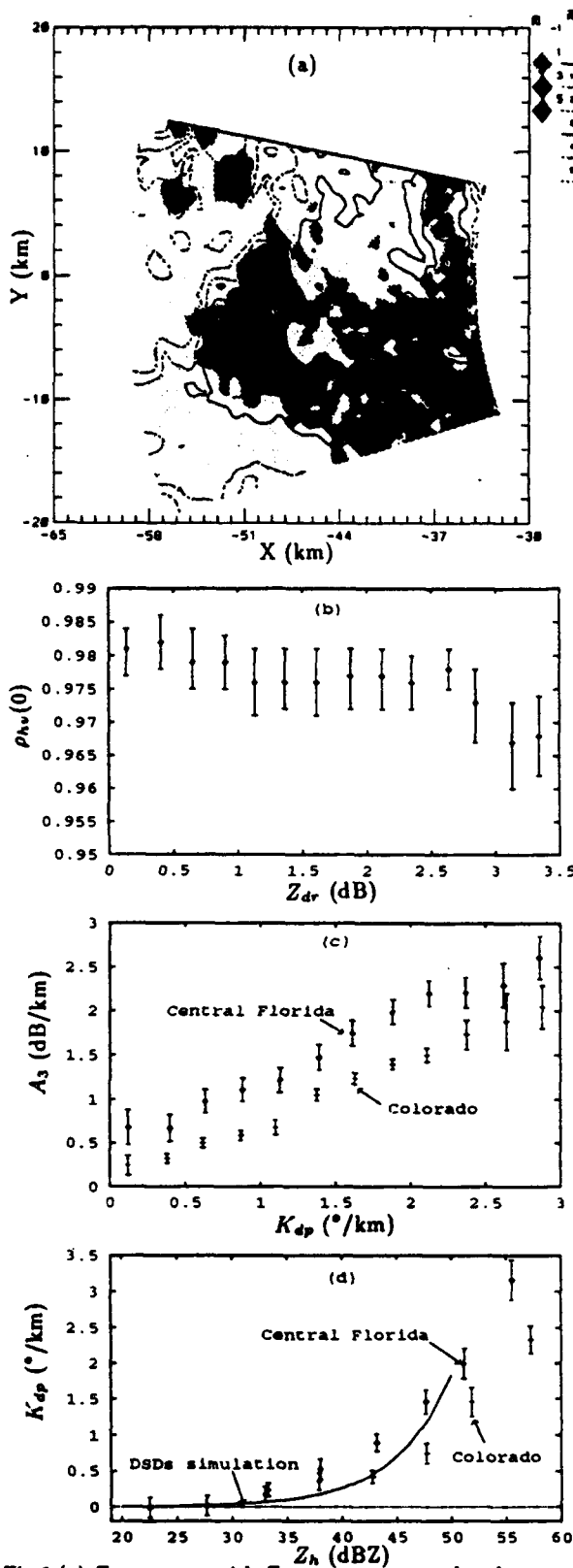


Fig.2 (a)  $Z_h$  contours with  $Z_{dr}$  grey scales overlaid; (b) mean and 95% C.I. of  $\rho_{hv}(0)$  vs  $Z_{dr}$ ; (c) mean and 95% C.I. of  $A_3$  vs  $K_{dp}$ ; (d) mean and 95% C.I. of  $K_{dp}$  vs  $Z_h$ .

On 24 August 1991 a squall-line approached the radar from the W-NW.  $Z_h$ ,  $Z_{dr}$ , DFR,  $\phi_{dp}$  and  $\rho_{hv}(0)$  have been filtered in range using an IIR filter which sharply attenuates spatial fluctuations 250 m and less.

Fig.2a shows a PPI scan of  $Z_h$  at 1.5° elevation angle derived from the central Florida data. Grey scales correspond to  $Z_{dr}$  with darker shades representing higher values.

Fig.2b shows a plot of  $\rho_{hv}(0)$  vs  $Z_{dr}$  obtained from the 1.5° elevation PPI in Fig.2a between 38 - 48 km. The mean  $\rho_{hv}(0)$  does decrease with increasing  $Z_{dr}$  in agreement with theory, but the  $\rho_{hv}(0)$  values are significantly lower compared to both theory and the experimental results of Illingworth & Caylor (1991). We refer to Xiao et al. (these Proceedings) for a further discussion of antenna effects related to the lowered values of  $\rho_{hv}(0)$ .

Fig.2c shows  $A_3$  vs  $K_{dp}$  in rain from data collected at 1.5° elevation (37 - 48 km) and subsequently, at elevation angles 2 - 4° (14 - 26 km). The mean and 95% confidence intervals are shown in Fig.2c and are marked as data from central Florida. Another curve marked 'Colorado' is CP-2 time series data from a rainshaft in a Colorado storm at low elevation angle (1°) at range 82 - 93 km. These data have been processed exactly the same as for the central Florida data. In the  $K_{dp}$  range 1 - 2.25° km<sup>-1</sup>, the two data sets have different slopes; the central Florida data has a slope of 1.05 while the Colorado data has a slope of 0.78. Also, for a given  $K_{dp}$ , the  $A_3$  values in Colorado are consistently less than in central Florida. We believe that these features are statistically significant and are a manifestation of microphysical differences between the two regimes, principally related to drop size distributions, and secondarily to mean raindrop shape vs size relations. The Colorado slope of 0.78 is very close to that predicted theoretically by Bringi et al. (1990) for Gamma DSDs (0.8), and for experimental DSDs (collected in Norman, OK) from surface distrometer (0.79) assuming equilibrium raindrops shape vs size relation due to Green (1975). The results from Fig.2c are independent of absolute system gain and as a consequence are more reliable.

Fig.2d shows the mean  $K_{dp}$  vs  $Z_h$  for the central Florida and Colorado datasets. The solid line is the mean relationship from simulations using Gamma DSDs. Again, for a given  $K_{dp}$ , the  $Z_h$  in Colorado is as expected larger than in central Florida.

### 2.3. Vertical Cross Sections through A Squall Line

We now show vertical cross sections through the most intense part of the 24 August squall line. Fig.3 shows an RHI scan taken to the west of the radar. Darker shades represent higher values of  $Z_{dr}$  and  $A_3$ . Contours start at 10 dBz and increment by 10 dBz. These data were collected in the normal operating mode of the CP-2 radar which does not allow for computation of differential phase and  $\rho_{hv}(0)$ . Fig.3a shows  $Z_h$  contours with  $Z_{dr}$  grey scales overlaid, while Fig.3b show contours of  $Z_h$  with  $A_3$  overlaid. The leading edge of the squall line is at 18 km range. Note the positive  $Z_{dr}$  column at 22 km, with the

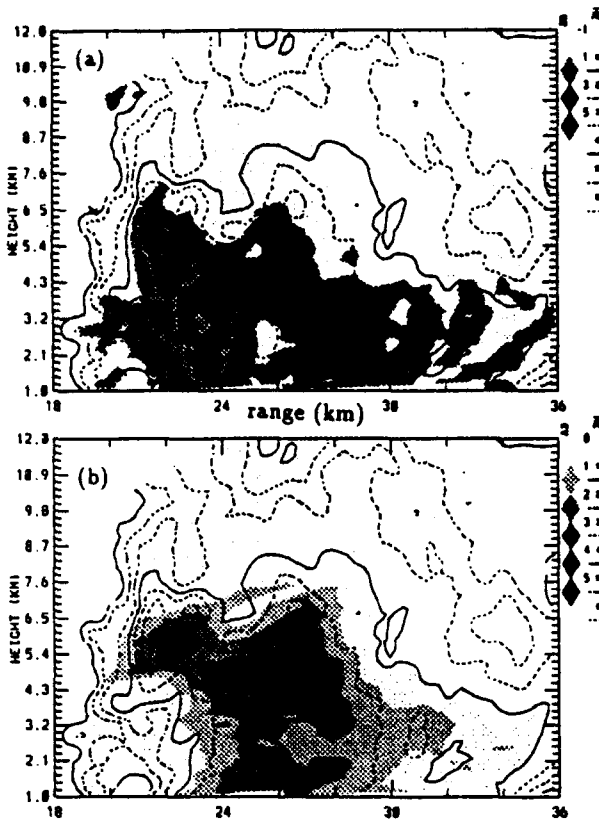


Fig.3  $Z_h$  contours with (a)  $Z_{dr}$ , (b)  $A_3$ , grey scales overlaid.

2 dB contour reaching 6.5 km agl. The peak  $Z_{dr}$  is 4.5 dB at 5 km agl. The  $A_3$  core is located at 4.5 km agl in Fig.3b in the range sector 24 - 27 km where  $Z_{dr}$  is 1.5 - 2.0 dB. This  $A_3$  core represents the main precipitation mass. On the inflow side, a secondary  $A_3$  maximum can be located at 6 km agl in the range 22 - 23 km which also coincides with high  $Z_h$  (60 dBZ) and high  $Z_{dr}$  (3.5 - 4 dB). This region consists of large raindrops suspended by the updraft.

About 3 minutes later, time series data were collected through the same storm at the same location as described in Fig.3. Range profiles at elevation angle  $11^\circ$  are shown in Fig.4. This profile intersects the main precipitation mass shown in Fig.3b at 4.7 km agl, range = 25 km. Fig.4a,b shows range profiles of  $Z_h$ ,  $Z_{dr}$ ,  $\phi_{dp}$  and  $K_{dp}$ . Note the peak  $K_{dp}$  of  $4.75^\circ km^{-1}$  corresponding to a rainfall rate of  $150 mm h^{-1}$ . Note the decrease in  $Z_{dr}$  from 3.75 dB at 23.5 km to 0.5 dB at 29 km, indicating the transition from rain to ice. Fig.4c,d show range profiles of  $Z_h$ ,  $\rho_{hv}(0)$ , DFR and  $A_3$ . From 23 to 29 km,  $\rho_{hv}(0)$  (unfiltered in range) decreases from 0.98 to 0.93 indicating a transition from rain to ice. Beyond 30 km, the average  $\rho_{hv}(0)$  is 0.96, and beyond 35 km it is 0.985. The peak  $A_3$  is  $4.7 dB km^{-1}$  and its location coincides with the peak  $K_{dp}$  location. The DFR curve decreases with range from 30 km onwards as the X-band signal falls below noise level due to attenuation.

### 3. CONCLUSIONS

Vertical incidence data in light rain revealed a dip in

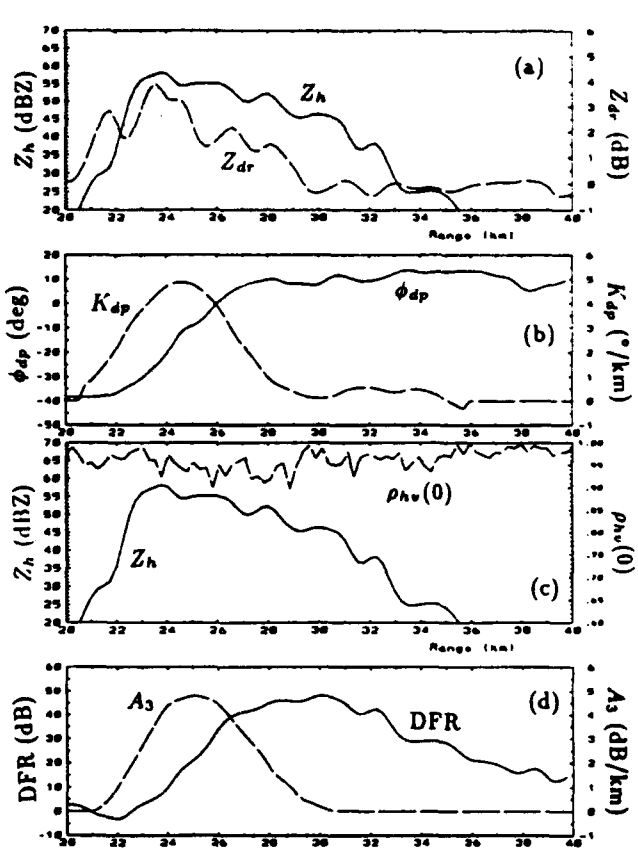


Fig.4 Range profiles of (a)  $Z_h$  and  $Z_{dr}$ ; (b)  $\phi_{dp}$  and  $K_{dp}$ ; (c)  $Z_h$  and  $\rho_{hv}(0)$ ; (d) DFR and  $A_3$ .

$\rho_{hv}(0)$  just below the bright-band, as well as weak Mie scattering effects. The accuracy in estimating  $A_3$  and  $K_{dp}$  (from the vertical incidence data) was established to be  $0.2 dB km^{-1}$  or  $^\circ km^{-1}$ .

Data from central Florida and Colorado were compared in convective rainfall which showed differences attributable to drop size distribution variations and to a lesser extent variations in the mean raindrop shape vs size relation.

Vertical sections of data through the intense portion of a squall line revealed interesting microphysical features such as a positive  $Z_{dr}$  column adjacent to the leading edge, the transition from rain to 'rain + ice' to ice as revealed by  $\rho_{hv}(0)$ , and the large values of  $A_3$  and  $K_{dp}$  within the main precipitation mass.

#### Acknowledgement

Support for this research came from the National Science Foundation via ATM-9014600 and from AFOSR via AFOSR-91-0141.

#### References

- Bringi et al., 1990: *J. Atmos. Oceanic Tech.*
- Green et al., 1975: *J. Appl. Meteor.*, (14)
- Hubbart et al., 1993: (to appear) *J. Tech.*
- Illingworth et al., 1991: *25th Conf. Radar Meteor.*
- Liu et al., 1993: *26th Int. Conf. Radar Meteor.*
- Xiao et al., 1993: *26th Int. Conf. Radar Meteor.*

## MICROPHYSICAL AND ELECTRICAL EVOLUTION OF A CONVECTIVE STORM USING MULTIPARAMETER RADAR AND AIRCRAFT DATA DURING CaPE

V.N. Bringi, I.J. Caylor, J. Turk and L. Liu  
Colorado State University, Fort Collins, CO 80523

### 1. INTRODUCTION

On 9 August 1991 of the CaPE project the transition from early echo to mature stage was captured by the CP-2 radar as well as two King Airs (NCAR KA and Wyoming KA), the NOAA P-3 and the T-28 aircrafts. It was the only such case in CaPE involving good coordination between the multiple aircraft and radar permitting a study of the microphysical and electrical evolution of the particular cloud. A companion paper by Bringi et al. (these Proceedings) deals with the evolution of another adjacent cloud (about 7 km away) which was penetrated by the T-28. The general environmental conditions were quite similar for both clouds and we refer to that paper for details. However, the microphysical evolution has some differences between the two clouds that are interesting.

The cloud was first detected (peak of 3 dBZ at height = 2.6 km and range = 25 km) at 17:48 UTC (henceforth all height are msl and time are UTC). The dual-frequency (S/X-band) reflectivity ratio, DFR, was 15 dB indicating dominance by Bragg scattering. At 17:51, the peak reflectivity increased to 22.5 dBZ, DFR decreased to 0 dB and  $Z_{dr}$  increased to 0.75 dB, evidence of coalescence formation of drops. About 10 minutes later (18:00) a strong positive  $Z_{dr}$  column had formed, similar to those reported by Illingworth (1992) in Alabama during MIST. The warm cloud with a positive  $Z_{dr}$  column persisted until 18:09 and then the cloud glaciated, releasing latent heat and accompanied by strong vertical growth. A weak E-field ( $\sim 5$  kV/m) detected by NCAR KA at 18:12 forced it away from the cloud. An enhanced E-field was detected by the NOAA P-3 at 18:16. The first cloud-to-ground lightning from the cloud was detected by the NASA LLP network at 18:18.

### 2. CLOUD EVOLUTION

Surface winds were from the W/NW near the Cape. The 15:00 sounding at Cape Canaveral indicated light westerly winds up to 6 km turning E/SE above 7.5 km. The  $0^\circ\text{C}$  level was at 4.6 km, with cloud base near 1.2 km. The LWC observations from aircraft were less than  $1 \text{ g/m}^3$  indicating a large amount of mixing in these clouds (adiabatic LWC from sounding was  $\sim 6 \text{ g/m}^3$ ).

The cloud (A) of interest was detected (17:55) about 4 km NW of another cloud (B) that was in a more mature phase. Both clouds were about 10 km NE of an intense convective line of thunderstorms. At 18:01, cloud B's reflectivity core ( $\sim 47$  dBZ at 4.5 km) started to descend while the now glaciated upper part of the cloud (4 - 7 km) began to tilt to the NW in response to E/SE winds aloft.

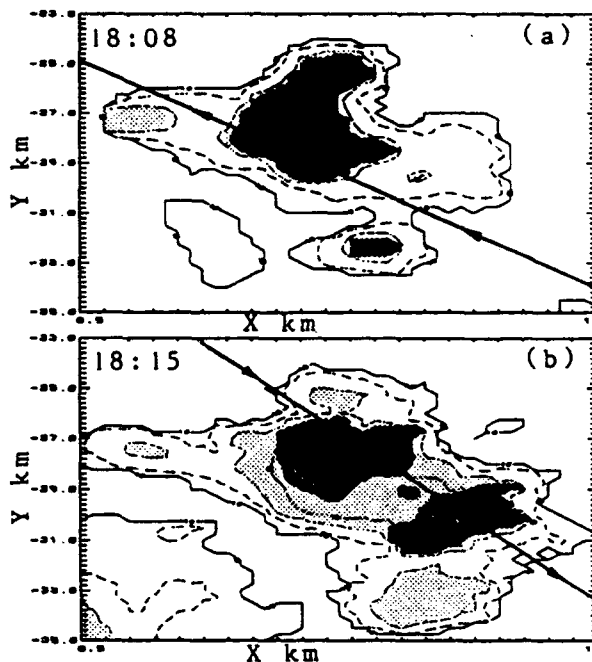


Fig.1 CAPPI at 5.5 km height of  $Z_h$  contours with  $Z_{dr}$  grey scales. Darker shades are larger  $Z_{dr}$ , the intervals being .5,1.5,3,4 dB.

At 18:04, the warm cloud A which was on the up-shear side (top  $\sim 5$  km) had the tilted upper part of cloud B overhead. It is possible that surface outflow from cloud B enhanced low level convergence near cloud A. It is also possible that tiny ice crystals or graupel from cloud B may have descended and melted into cloud A forming tiny drops that can grow quickly to very large raindrops. Indeed at 18:08 the 3 dB  $Z_{dr}$  contour in cloud A reached up to 6 km, with maximum  $Z_{dr}$  of 4 dB at 4 km height (prior to this the maximum  $Z_{dr}$  was 2.5 dB at 3 km, and cloud top was 5 km). Also, cloud B loses its identity after 18:05, more or less merging with cloud A.

Fig.1a,b show CAPPI of cloud A at 5.5 km height at (a) 18:08 and (b) 18:15; contours of  $Z_h$  start at 10 dBZ and increment by 10 dB while  $Z_{dr}$  is shown as a grey scale with darker shades representing larger  $Z_{dr}$ . Cloud A is centered at X=13, Y=-27 km in Fig.1a which also shows the positive  $Z_{dr}$  column. In Fig.1b the strength of the column has weakened considerably. The NOAA P-3 penetrations at 18:09 and 18:15 are shown in Fig.1. Figs.2a,b,c show vertical sections taken along a line oriented SE-NW ( $132^\circ$  from N) in Fig.1; positive (negative) X represents distance SE (NW) from the core. The positive  $Z_{dr}$  column in Fig.2a is clearly visible at 18:08, while at 18:12

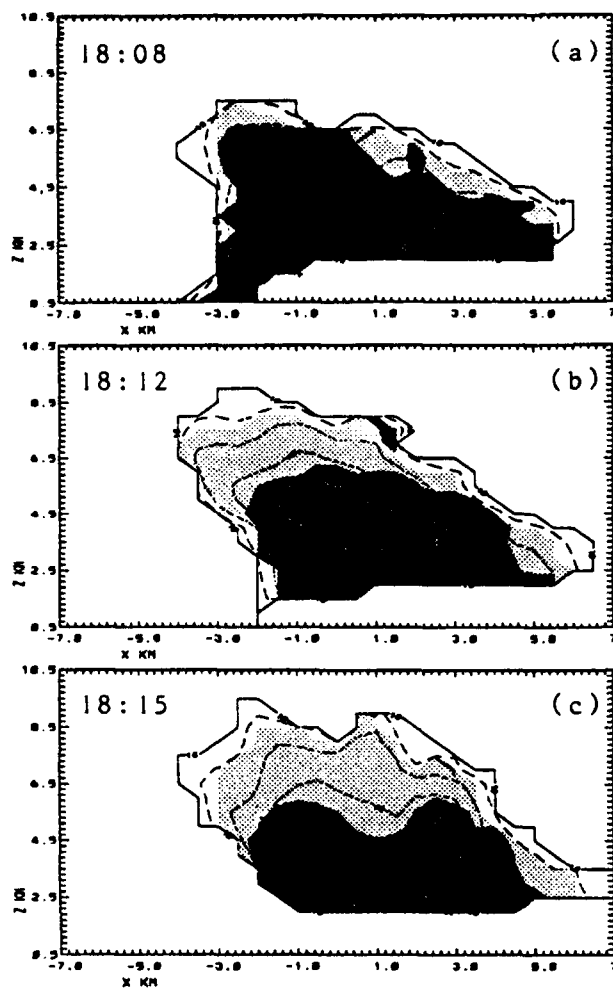


Fig.2 Vertical sections along an SE - NW line in Fig.1.  $X=0$  here is the center of the core in Fig.1.  $Z_{dr}$  grey scales same as in Fig.1.

(Fig.2b) the cloud has glaciated. At 18:15 the reflectivity core was descending and the  $Z_{dr}$  structure conforms to the more usual ice-melting-drops situation.

The NOAA P-3 made its penetrations at an altitude of 6.4 km ( $-10^{\circ}\text{C}$ ). Fig.3 shows some of the aircraft measured data during the 18:09 (solid line) and 18:15 (dashed line) penetrations. The top panel shows up/downdraft and liquid water content (LWC), while the bottom panel shows the vertical E-field. At 18:09 the P-3 (going SE  $\rightarrow$  NW) was flying on top of the positive  $Z_{dr}$  column (shown in Fig.2a). The main precipitation core ( $Z_h \sim 50$  dBZ) was located about 1 km below the flight altitude. Peak  $Z_{dr}$  ( $\sim 3$  dB) was located at 4.4 km. The updraft location coincides well with the positive  $Z_{dr}$  column. Before encountering the updraft (from the SE side of core) the 2D-C probe showed rough edged graupel (maximum dimension  $\sim 2$  mm). Upon entering the updraft, the images were very smooth with particle types being drops and wet graupel. A 3 mm raindrop was detected in the center of the second updraft peak ( $\sim 70$ s from 0 in Fig.3). Within the updraft region a high LDR layer was detected

with values around -17 dB with X-band specific attenuation ( $A_3$ ) of 1 dB/km.  $Z_{dr}$  was around 1 - 1.5 dB. The large LDR signature indicates wet graupel while both  $Z_{dr}$  and  $A_3$  are indicative of supercooled drops consistent with the 2D-C images. The E-field is very weak at 18:09.

The NCAR and Wyoming King Air (NKA, WKA) each made a NW  $\rightarrow$  SE penetration ( $-3^{\circ}\text{C}$ ,  $2.3^{\circ}\text{C}$ ) centered at 18:11. At this time (Fig.2b) the cloud glaciated with cloud top rising from 7.5 km (at 18:08) to 9.0 km (at 18:12). The NKA's penetration at 5.5 km went just on top of the column while the WKA was in the high  $Z_{dr}$  region (3 - 3.5 dB) at 4 km height (Fig.2b). The NKA detected a peak updraft of 8 m/s on top of the column and downdraft peak of -3 m/s adjacent to it. At this flight level, a layer of high LDR (-18 to -20 dB) and  $A_3$  (1 - 1.5 dB/km) was noted at the up/down transition. The NKA detected fields of 5 - 6 kV/m and soon exited the cloud. The WKA at lower altitude (4 km) detected a peak updraft of 9 m/s followed by a peak downdraft of -4 m/s separated by 900 m. Large drops (5 - 7 mm) were detected by the P-probe during this penetration.

The P-3 made its reverse penetration (going NW  $\rightarrow$  SE) at 18:15 with data shown in Fig.3. The vertical velocity has decreased substantially and the E-fields have increased dramatically. Fig.2c shows the vertical  $Z_{dr}$  structure. At the P-3 flight level (6.4 km),  $Z_{dr}$  is nearly 0 dB while LDR is -26 dB and  $A_3$  is near zero. The storm is in its mature phase and the main precipitation core ( $Z_h$  peak of 57 dBZ) is descending to the surface. The 2D-C probe detects a much higher concentration of rough-edged graupel (maximum sizes  $\sim 2 - 3$  mm).

Fig.4 shows a time-height cross section of cloud evolution from first echo (17:48:00 is  $t=0$ ) through a 30 min period. The dark solid line is the maximum height reached by the 2 dB  $Z_{dr}$  contour. Note the maximum height of 6 km reached at  $\sim 18:08$  (1250s from  $t=0$ ) following which there is a steady decrease to 2 km. The vertical arrows represent updraft detected by the P-3 (6.5 km), NKA (5.5 km) and T-28 (4.8 km) at various times in the cloud evolution. The updraft magnitude decreases with time are roughly correlated with the maximum height of the 2 dB  $Z_{dr}$  contour. The top panel shows the detection of the first cloud-to-ground lightning by the NASA LLP network at 18:18:12 at  $X=14.1$ ,  $Y=-29.5$  km (see Fig.1b). It appears that mixed phase microphysics plus the up/downdraft structure played important roles in electrifying the cloud. Detailed forthcoming analysis of all the aircraft data with radar LDR and  $A_3$  signatures will add important details to cloud microphysical and electrical evolution. This study can be compared to another cloud evolution described by Brangi et al. (these Proceedings).

#### Acknowledgement

Support for this research came from the NSF via ATM-9014600 and from AFOSR via 91-0141. Useful discussion with Dr. Detwiler of SDSM&T are acknowledged.

#### References

- Brangi et al., 1993: 26th Int. Conf. Radar Meteor.
- Illingworth, 1992: Proc. 11th Int. Conf. Clds. Precip., (1)

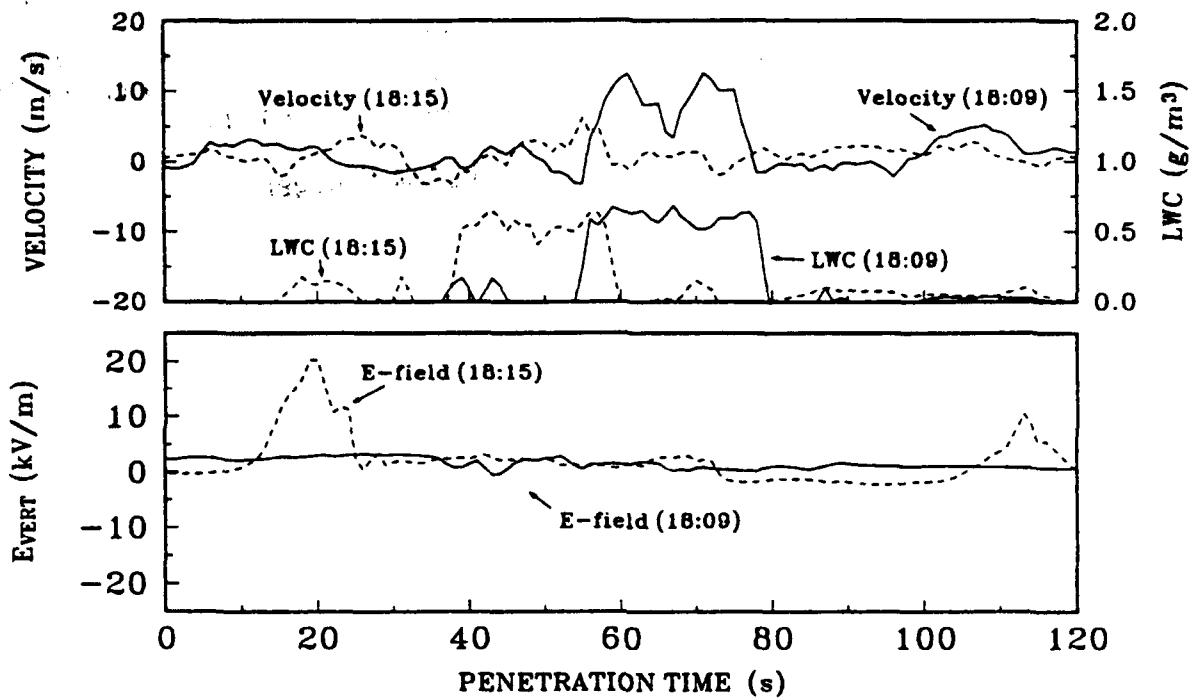


Fig.3 Data from NOAA P-3 showing up/downdraft (velocity), liquid water content (LWC) and vertical E-field. The time  $t=0$  is the starting time for each penetration.

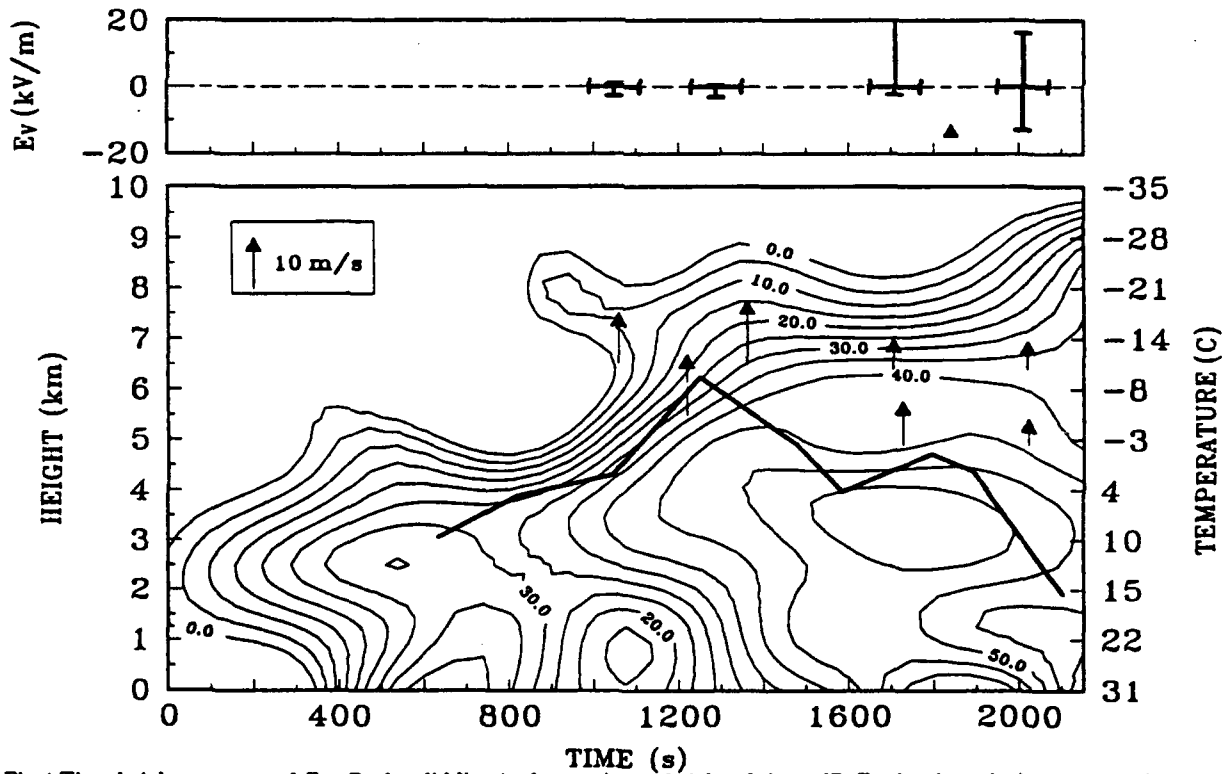


Fig.4 Time-height contours of  $Z_h$ . Dark solid line is the maximum height of the 2 dB  $Z_{dr}$  level reached at various times. Vertical arrows are updraft speeds from various aircraft. Top panel shows vertical E-field from P-3. The solid triangle mark at 1840s is the first CG strike.